Biomaterials 337 (2027) 124495



Contents lists available at ScienceDirect

Biomaterials

journal homepage: www.elsevier.com/locate/biomaterials





Multifunctional theranostic nanocarrier platform for microglia-selective cytochalasin D delivery to modulate neuroinflammation after acute brain injuries

Sabri E.M. Sahnoun [a,b], Rozina Noristani [c], Paolo Alimonti [b,d], Jonas Pes [e], Lara Gubeljak [e], Annika Szymura [f], Shaista Ilyas [f], Eren Arik [e], Alexandru Florea [a,g], Eva M. Buhl [h], Bernd Neumaier [i,j], Sanjay Mathur [f], Jörg B. Schulz [e,k], Felix M. Mottaghy [a,g], Pardes Habib [c,e,*]

[a] Department of Nuclear Medicine, University Hospital Aachen, RWTH Aachen University, Aachen, 52074, Germany
[b] Department of Oncology, University of Oxford, Oxford, OX3 7DQ, United Kingdom
[c] Department of Neurosurgery and Stanford Stroke Center, Stanford University School of Medicine, Stanford, CA, 94305, USA
[d] Department of Neurosurgery, Brigham and Women's Hospital, Harvard Medical School, Boston, MA, 02120, USA
[e] Department of Neurology, University Hospital Aachen, RWTH Aachen University, Aachen, 52074, Germany
[f] Institute of Inorganic and Materials Chemistry, University of Cologne, Cologne, 50939, Germany
[g] Department of Radiology and Nuclear Medicine, Maastricht University Medical Center, Maastricht, 6202, The Netherlands
[h] Electron Microscopy Facility, Institute of Pathology, University Hospital Aachen, RWTH Aachen University, Aachen, 52074, Germany
[i] Institute of Radiochemistry and Experimental Molecular Imaging, University Hospital Cologne, University of Cologne, Cologne, 50937, Germany
[j] Institute of Neuroscience and Medicine, Forschungszentrum Jülich GmbH, Jülich, 52425, Germany
[k] JARA-BRAIN Institute of Molecular Neuroscience and Neuroimaging, Forschungszentrum Jülich GmbH and RWTH Aachen University, Aachen, 52074, Germany

ARTICLE INFO

Keywords:
Precision medicine
Nanomedicine
Theranostics
Targeted drug delivery
Neurotherapeutics
Stroke
TBI

ABSTRACT

Targeting microglia to modulate neuroinflammation after acute brain injuries (ABIs) is promising but limited by poor blood-brain barrier (BBB) penetration and systemic toxicity of candidate agents. In addition, multifunctional platforms combining targeted therapy with real-time traceability remain limited. We developed and characterized a multifunctional theranostic, folate-functionalized, polydopamine (PDA)-coated mesoporous silica nanoparticle (FA-NP) system for microglia-selective delivery and intracellular release of cytoskeleton inhibitor Cytochalasin D (CytoD). FA-NPs exhibited ideal physicochemical properties for parenchymal brain accumulation and pH-sensitive PDA shells enabled intracellular retention and gradual degradation. Using radiolabeled and fluorescein-isothiocyanate-functionalized FA-NPs, SPECT/CT imaging, γ-counting, autoradiography, and immunohistochemistry confirmed parenchymal brain accumulation with cellular uptake following systemic administration. Activated microglia upregulated folate receptors (FOLR1/2) and internalized FA-NPs *via* FOLR-mediated, dynamin-dependent endocytosis. CytoD-loaded FA-NPs (FA-NP[CytoD]) significantly reduced microglial migration, phagocytosis, ROS production, and proinflammatory cytokines, outperforming molecular CytoD while exhibiting notably lower toxicity compared to both CytoD and unfunctionalized particles. In organotypic brain slice models of hypoxia-reoxygenation and traumatic injury, FA-NP[CytoD] reduced inflammation at 24 and 96 h. Systemic administration enabled brain accumulation with clearance over time. Together, this multifunctional theranostic platform integrates selective microglial targeting, controlled drug release, and multimodal imaging, offering translational potential for ABIs.

* Corresponding author. Department of Neurosurgery and Stanford Stroke Center Stanford University School of Medicine, 1201 Welch Road, MSLS P352, Stanford, CA, 94305-5487, USA.
E-mail address: phabib@stanford.edu (P. Habib).

https://doi.org/10.1016/j.biomaterials.2026.124495
Received 17 January 2026; Received in revised form 1 June 2026; Accepted 26 July 2026
Available online 29 July 2026
0142-9612/© 2026 The Authors. Published by Elsevier Ltd. This is an open access article under the CC BY license (http://creativecommons.org/licenses/by/4.0/).

1. Introduction

Neurological disorders are a major global health challenge, accounting annually for about 11 million deaths [1]. Their prevalence has risen steadily over the past three decades, now affecting nearly one in two individuals across lifespan [2]. Among these conditions, acute brain injuries (ABIs), such as stroke and traumatic brain injury (TBI), stand out as particularly devastating, becoming a leading cause of chronic disability in adults worldwide [3]. A major obstacle to therapeutic intervention in these conditions is the blood-brain barrier (BBB), which inhibits the entry of over 98 % of small molecules and nearly all macromolecular therapeutics to the brain parenchyma [4–6]. Consequently, the development of therapies for ABIs is constrained, emphasizing the need for strategies that enable targeted delivery to injured brain regions [7–9]. Accordingly, there is a growing need for multifunctional nanomedical systems that not only enable brain delivery, but also combine cell-selective targeting, controlled drug release, and non-invasive *in vivo* monitoring of biodistribution.

Microglia, the resident macrophage-like cells of the central nervous system (CNS), are the primary responders to CNS injury and have emerged as key targets in several neurological diseases [10,11]. Derived from yolk-sac progenitors, microglia populate the CNS early in development, maintaining themselves throughout life by self-renewal mechanisms. These distinct immune cells make up 10 % of the total cell population in the brain [12–14]. Under homeostatic conditions, microglia contribute to synaptic pruning, debris clearance, neurogenesis, myelination, and immune surveillance [14,15]. Following brain injury, microglia rapidly detect damage-associated molecular patterns released by damaged neurons and shift toward a reactive phenotype characterized by the secretion of pro-inflammatory cytokines, chemokines and reactive oxygen species (ROS) [16–18]. While microglial responses aim to restore homeostasis after CNS injury, excessive or prolonged activation can result in secondary neuronal damage and exacerbates neurodegeneration [13,19–22]. Consequently, selective modulation of microglial activity, without ablation, represents a promising therapeutic strategy for mitigating neuroinflammatory damage [23]. Such integrated strategies may be particularly valuable in ABIs, where treatment timing, spatial precision, and dynamic inflammatory responses critically influence outcome.

Cytochalasin D (CytoD), an actin polymerization inhibitor, disrupts microglial functions such as migration and phagocytosis, thereby attenuating their activation and inflammatory response [24–26]. However, the pronounced systemic toxicity and inability of CytoD to cross the BBB have precluded its clinical testing [27]. To overcome these limitations, biocompatible nanotechnology-based delivery systems offer promising potential for transporting drugs into the brain with both spatial and cellular precision. Among available platforms, mesoporous silica nanoparticles ($mSiO_2$-NPs) enable a tunable architecture for drug loading and functionalization. Their versatile nature allows efficient encapsulation of therapeutic agents, while tailored surface modifications enhance circulation time, targeting capacity, and control over drug release [28–31]. However, uncoated silica particles have been associated with dose-dependent cytotoxicity, microglial stress and inflammatory responses, highlighting the need for biocompatible surface modifications to ensure safety [32–39].

Polydopamine (PDA) coatings on nanocarriers represent a robust strategy to improve nanoparticle biocompatibility, offering high serum stability, extensive drug loading capacity, and pH-sensitive release in acidic environments such as endolysosomal compartments [40–45]. In addition, PDA-coated NPs, and not bare silica NPs have been shown to cross the BBB and attenuate neuroinflammation in rodent models [46,47].

Upon activation, microglia upregulate folate receptors (FOLR 1/2), which makes folic acid (FA) an effective target ligand for selective drug delivery to these cells [48–50]. FA-functionalized PDA-coated NPs present a promising theranostic (loaded drug + imaging moieties) approach to enhance selective uptake by reactive microglia while minimizing off-target effects [48–50]. However, despite the growing interest in PDA-coated NPs, our understanding of their cellular uptake dynamics, intracellular trafficking, subcellular biodistribution, and retention times in brain-resident cells remains incomplete. Limited understanding about the transport of PDA-coated NPs across the BBB, the mechanisms underlying their selective uptake by activated microglia, and the spatiotemporal regulation of drug release within the CNS hinders their clinical translation and rational design as PDA-modified nanotherapeutics for neurological applications.

Here, we introduce a multifunctional theranostic nanocarrier platform based on radio- or FITC-labeled PDA-coated, FA-functionalized $mSiO_2$ nanoparticles (FA-NPs) designed to combine microglia-selective targeting, controlled intracellular CytoD release, and multimodal fluorescence or emission tomography imaging, to address these gaps and enable targeted theranostic modulation of microglia in acute brain injury. Our system enables dual radiolabeling with Gallium-68 (^{68}Ga) for positron emission tomography combined with computed tomography (PET-CT) and Lutetium-177 (^{177}Lu), while encapsulating CytoD for localized immunomodulation. We chose the gamma- and beta-emitting radionuclide ^{177}Lu for its long half-life (6.7 d), allowing for prolonged intracellular tracking and single-photon emission computed tomography with computed tomography (SPECT/CT) to investigate trafficking and biodistribution mechanisms. This was complemented by ^{68}Ga, a short-lived PET nuclide (67 min), for early-phase imaging. Given the delayed onset of radiation-induced damage, the short experimental duration, low CNS cell proliferation, and the minimal non-therapeutic dose [<0.01 Bq/cell], potential ^{177}Lu-induced radiotoxic effects were unlikely to interfere with the mechanistic insights provided in this study. The modularly engineered and radiolabeled nanoparticles exhibit uniform morphology, high radiochemical purity, and excellent serum stability. FA-NPs are predominantly internalized through FOLR-mediated, dynamin-dependent endocytosis by microglia in the brain, with uptake further enhanced upon activation. Once inside endolysosomal compartments, acidic degradation of the PDA shell enables pH-responsive CytoD release, leading to suppression of microglial migration, phagocytosis, and inflammatory cytokine expression. *In vivo* SPECT/CT, postmortem autoradiography (ARG), and immunohistochemistry (IHC) demonstrated efficient and homogenous parenchymal brain accumulation, intracellular uptake by CNS cells, and progressive clearance, demonstrating biocompatibility and translational potential.

Using *in vitro*, *in vivo,* as well as hypoxia-reoxygenation and focal brain injury models, we elucidate the cellular mechanism of nanoparticle uptake, drug release, biodistribution, and microglial immunomodulation. This work introduces modularly architected radio- or FITC-labeled FA-NP[CytoD] as a multifunctional nanotheranostic platform capable of microglia-directed modulation, real-time imaging, and controlled therapeutic delivery. By integrating receptor-mediated targeting, pH-sensitive payload release, and radiotracer-based biodistribution tracking, our system offers mechanistic insights into nano-bio interactions in the injured brain and introduces a strategy for precision neuroimmune modulation in CNS injury.

2. Results

2.1. Click- and DOTA-functionalized PDA-coated $mSiO_2$-NPs display tunability, high radiochemical yield, purity, and stability in human sera

To evaluate distinct functional aspects of the platform, dedicated NP variants were employed throughout the study depending on the experimental objective, including physicochemical characterization, mechanistic uptake studies, therapeutic cargo delivery, and fluorescence or radionuclide-based imaging. To engineer a multifunctional theranostic nanocarrier platform for microglia-selective drug delivery and imaging, we designed a modularly architected nanoparticle system integrating targeted uptake, pH-sensitive payload release, and fluorescence or

radionuclide-based tracking and imaging capabilities. The multi-functionalization, characterization, and stability of $mSiO_2$-NPs were successfully assured through a series of chemical modifications and a subsequent radiolabeling procedure. Bare $mSiO_2$ nanoparticles were synthesized *via* a template-assisted sol-gel process (TEOS), followed by polydopamine (PDA) coating to form PDA-NPs. Subsequently the NPs were conjugated with folic acid (FA) using carbodiimide chemistry to create PDA-capped and FA functionalized $mSiO_2$-NPs (FA-NPs). From this common carrier backbone, optional functional modules were introduced depending on the experimental objective, including DOTA conjugation for radiometal chelation, radiolabeling for quantitative intracellular tracking and nuclear imaging, FITC labeling for fluorescence imaging, and CytoD loading for therapeutic studies (Fig. 1A). The conjugation was confirmed through Fourier-transform infrared spectroscopy (FTIR) as previously shown [51], where the appearance of a peak at 1696 cm^{-1}, corresponding to the C═O vibration, indicated remaining carboxy groups post-FA conjugation, while a peak at 1604 cm^{-1} confirmed the presence of amide bonds formed during the coupling reaction (Fig. 1B). Zeta potential measurements further confirmed the successful functionalization of the nanoparticles. The surface charges shifted from −28.5 mV ($mSiO_2$-NP) to −41.2 mV (PDA-NP) and −37.5 mV (FA-NP) (Fig. 1B). Morphological characterization using transmission electron microscopy (TEM) revealed a spherical mesoporous structure with a mean diameter of approximately 110 nm for $mSiO_2$-NPs. PDA shell measurements revealed an average thickness of 29 nm with uniformly distributed pores (~4 nm in diameter). Furthermore, nanoparticle tracking analysis (NTA) detected hydrodynamic diameters in the range of 220-260 nm with polydispersity indices (PDI) below 0.15, indicating uniform size distribution across all three NP formulations (Fig. 1C–E). Radiolabeling was achieved by covalently attaching the radiometal chelator DOTA by conjugation of p–SCN–Bn-DOTA (S-2-(4-isothiocyanatobenzyl)-1,4,7,10-tetraazacyclododecane tetraacetic acid) with the NP surface, which allowed chelation of both the PET-imaging radionuclide ^{68}Ga (t ½ = 68 min) and the therapeutic radionuclide ^{177}Lu (t ½ = 6.7 d). Radio-TLC displayed radiolabeling conversions >98 % for both isotopes. The absence of a [^{68}Ga]Ga-DOTA or [^{177}Lu]Lu-DOTA peak at around 50 mm position of the TLC indicates that DOTA remained stably bound to the nanoparticle; such a peak would be expected if DOTA had dissociated (Fig. 1F and G). To exclude the possibility that the choice of radionuclide influences the nanoparticle uptake rate, we compared competitive uptake of [^{68}Ga]Ga-DOTA-PDA-NP and [^{177}Lu]Lu-DOTA-FA-NP (1:1) versus [^{177}Lu]Lu-DOTA-PDA-NP and [^{68}Ga]Ga-DOTA-FA-NP (1:1) in all three neuronal cells. The type of radionuclide appeared to have no impact on uptake rates in microglia, astrocytes, and neurons (Fig. S1A–D). Additionally, partition coefficient (logP) measurements using a γ-Counter revealed a calculated value of -3.31 ± 0.09, indicating the hydrophilic nature of the radiolabeled NPs (Fig. 1H). Optimal radiolabeling was observed at NP concentrations of ≥0.5 mg/mL for ^{68}Ga and ≥0.7 mg/mL for ^{177}Lu, with carrier concentrations reaching up to 0.15 ng (Lu)/μL (Fig. 1I). The stability of the radiolabeled NPs was further confirmed in human sera at 37 °C. Radio-TLC analysis demonstrated that the ^{68}Ga-labeled NPs remained stable (RCY >97 %) for over 3 h, while the ^{177}Lu-labeled NPs maintained stability (RCY >95 %) for up to 120 h (Fig. 1J and K). Furthermore, the radiolabeled ^{177}Lu-FA-NP formulation maintained high radiochemical stability under acidic conditions over a 12 h incubation period, corresponding to the relevant systemic circulation and accumulation window observed *in vivo*, thereby supporting the structural robustness of the DOTA-radiometal complex despite environmental pH changes (Fig. S1E). To further assess nanoparticle structural and morphological stability under CNS-relevant ionic conditions, FA-NPs or ^{177}Lu-FA-NPs were incubated in artificial cerebrospinal fluid (aCSF) for 24 h at 37 °C and pH 7.4. TEM analysis revealed preserved particle morphology and comparable particle size relative to control conditions, without evidence of degradation. Quantification of PDA shell mean thickness showed no significant difference compared to control conditions, supporting maintained structural and colloidal stability in a CSF-like environment (Fig. S1F and G). Furthermore, radiochemical stability analysis of ^{177}Lu-FA-NPs after 24 h incubation in aCSF and control media conditions revealed no significant differences, confirming preservation of radiochemical integrity under physiologically relevant aCSF conditions (Fig. S1H).

In summary, we modularly engineered $mSiO_2$-NPs functionalized with PDA and FA, and stably radiolabeled with ^{68}Ga and ^{177}Lu, achieving over 98 % labeling yield. Characterization confirmed uniform size, tunable functionalization, and high stability in human sera and preserved morphology and radiochemical stability in aCSF. Competitive uptake studies using two different radionuclides show no effect of the radionuclide type on uptake in brain cells, supporting their combined diagnostic and therapeutic potential.

2.2. *Activated microglia upregulate folate receptors and exhibit increased uptake of FA-functionalized NPs*

To evaluate the potential of FA-functionalized, PDA-coated $mSiO_2$-NPs (FA-NPs) for targeted drug delivery in neuronal cells, we visualized and quantified the intracellular uptake using ICC, TEM and γ-Counter (Fig. 2A–C). To visualize NP internalization, FITC-labeled FA-NPs (FITC-FA-NPs) were administered to microglia, astrocytes, and neurons for 1 h. ICC demonstrated that FITC-FA-NPs co-localized with cell-specific markers IBA1 (microglia), GFAP (astrocytes), and NeuN (neurons), indicating visual internalization across all three cell types (Fig. 2A–C, top panel). TEM analysis displayed internalized FA-NPs in all three cell types, predominantly localized within vesicular structures in cytoplasm and perinuclear regions. Notably, microglia exhibited a more dispersed vesicular distribution, with FA-NPs present in multiple endolysosomal compartments throughout the cytoplasm (Fig. 2A–C, middle panel). To quantify uptake rates of ^{177}Lu-labeled FA-NPs and PDA-NPs, we utilized a γ-Counter after 1 h of NP incubation. For all uptake experiments, a working concentration of 6.25 μg/mL NP suspension in cell culture medium was used, as dose-dependent LDH-release analyses confirmed preserved viability in microglia, astrocytes, and neurons at this concentration after 96 h (Fig. S2D–F). Initial concentration-dependent uptake analyses in microglia further demonstrated significantly increased FA-NP uptake at 6.25 μg/mL compared to lower concentrations, whereas higher concentrations (12.5 and 25 μg/mL) did not further increase uptake, indicating a saturation-like effect of nanoparticle internalization (Fig. S2H). Additional dose-dependent FA-NP uptake experiments in astrocytes and neurons revealed no significant concentration dependency in astrocytes, whereas neurons exhibited significantly increased uptake only at concentrations above 6.25 μg/mL (Fig. S2I and J). To mimic an inflammatory/activated state of neuronal cells, we subjected all three cell types to lipopolysaccharide (LPS) treatment [1 μg/mL] or vehicle for a total of 3 h (Fig. 2A–C, bottom panel). To investigate the effect of surface functionalization, we compared the uptake rates of unfunctionalized, PDA-coated $mSiO_2$-NPs (control: PDA-NP) and FA-functionalized, PDA-coated $mSiO_2$-NPs (FA-NPs) across all three cell types. A significant increase in uptake was observed exclusively in microglial cells following FA functionalization ($p < 0.001$). Microglia also displayed the highest uptake rates of FA-NPs (~40 %), followed by astrocytes (~20 %) and neurons (~11 %). Notably, LPS treatment further increased microglial uptake of FA-NPs (~48 %, $p < 0.05$), whereas LPS had no effect on FA-NP uptake in astrocytes and neurons (Fig. 2A–C, bottom panel). Exposure to acidic conditions (pH 5.0) additionally increased microglial uptake of ^{177}Lu-PDA-NPs compared to physiological pH 7.4 ($p < 0.05$). Notably, ^{177}Lu-FA-NPs exhibited an even more pronounced uptake enhancement under acidic conditions, reaching a significance level of $p < 0.001$ relative to pH 7.4 (Fig. S2C). To further investigate the enhanced uptake of FA-functionalized NPs in microglial cells, we performed TEM imaging to visualize the internalization of bare $mSiO_2$-NPs, PDA-NPs, and FA-NPs, and assessed folate receptor expression using ICC and Western blot

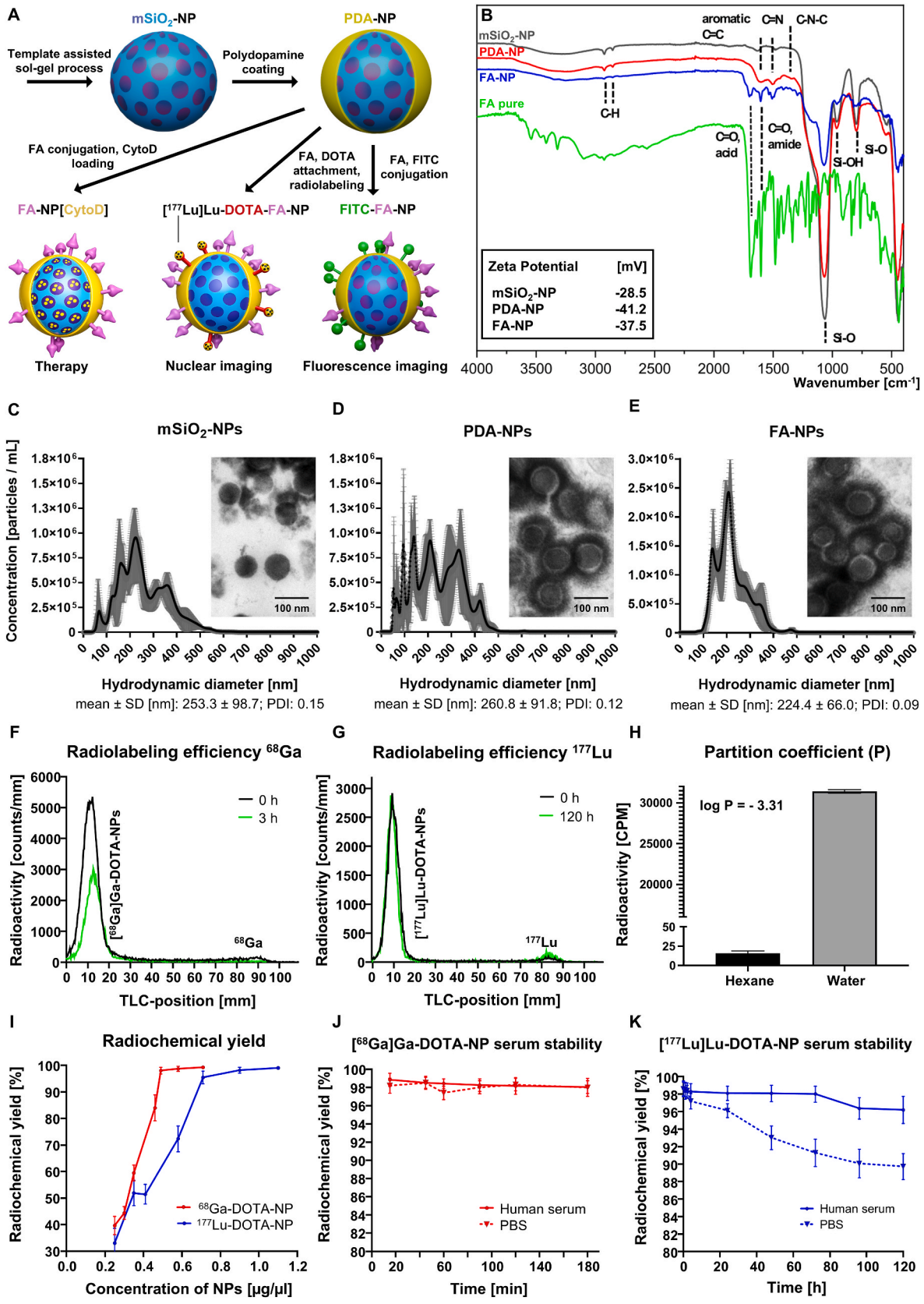

(caption on next page)

Fig. 1. Modular Chemical and radiochemical functionalization, characterization, and stability of a multifunctional theranostic $mSiO_2$ nanoparticle platform. **(A)** Schematic illustration of template-assisted sol-gel synthesis of $mSiO_2$-NPs, surface coating with polydopamine (PDA) to generate PDA-NPs, carbodiimide coupling reaction for the conjugation of folic acid on PDA-capped $mSiO_2$-NPs (FA-NP), followed by FITC-labeling, chelator (DOTA) attachment, CytoD loading and radiolabeling with the theranostic pair ^{68}Ga and ^{177}Lu. **(B)** FT-IR spectra of $mSiO_2$ (black), PDA-NP (red), FA-NP (blue), and pure FA (green) modified from Ilyas et al. [51]. The surface charges (zeta potential) for the bare and functionalized $mSiO_2$-NPs in water at pH 7 in triplicates are shown in table. **(C–E)** The hydrodynamic diameter [nm] and polydispersity index (PDI) were assessed using nanoparticle tracking analysis (NTA). Representative TEM images of $mSiO_2$-NPs and their functionalized derivatives are presented. The radiolabeling efficiency of ^{68}Ga- **(F)** and ^{177}Lu- **(G)** labeled NPs were assessed utilizing radio-thin layer chromatography (radio-TLC). **(H)** Evaluation of the lipophilicity/partition coefficient (P) and the calculated logP value of NPs were measured using a gamma counter (γ-Counter). **(I)** Radio-TLC analysis of the concentration-dependent radiochemical yield (RCY) of ^{68}Ga- and ^{177}Lu-labeled NPs ([^{68}Ga]Ga-DOTA-NP = ^{68}Ga-DOTA-NP; [^{177}Lu]Lu-DOTA-NP = ^{177}Lu-DOTA-NP). To determine the serum stability, ^{68}Ga- **(J)** and ^{177}Lu- **(K)** labeled NPs were measured in human sera and PBS control in a time-dependent manner. Data are shown as means ± SD of 3 independent experiments with 3 technical replicates. (For interpretation of the references to color in this figure legend, the reader is referred to the Web version of this article.)

analysis (Fig. 2D–J). Consistent with our previous findings, FA functionalization led to markedly increased intracellular accumulation compared to bare $mSiO_2$-NPs and PDA-NPs (Fig. 2D and E). Microglial cells expressed both folate receptors (FOLR1/FOLR2), and Western blot quantification revealed a significant upregulation of both receptors upon LPS stimulation ($p < 0.05$). Although FOLR2 is expected to be predominantly membrane-associated, with additional intracellular/endosomal localization reported following receptor internalization, the ICC signal in our 2D images was interpreted as evidence of cellular FOLR2 expression rather than definitive subcellular localization; this was further supported by Western blot analysis showing FOLR2 at the expected molecular weight. To further validate the modular imaging configuration, an additional quantitative uptake study using ^{177}Lu-DOTA-FITC-FA-NPs and the corresponding control formulation ^{177}Lu-DOTA-FITC-PDA-NPs was performed in microglial cells, confirming enhanced intracellular accumulation after FA functionalization and thereby supporting the targeting advantage of the combined radiolabeled/fluorescent nanoparticle platform (Fig. S1I).

In conclusion, FA-NPs are preferentially internalized by microglia, and this uptake is further amplified by microglial activation, which is accompanied by upregulation of folate receptors FOLR1 and FOLR2. This activation-dependent enhancement is specific to microglia and not observed in astrocytes or neurons. The vesicular localization of internalized particles suggests uptake through an endolysosomal pathway, potentially involving folate receptor–mediated endocytosis.

2.3. Microglia rapidly internalize FA-NPs predominantly via FOLR- and dynamin-dependent endocytosis

To investigate cellular uptake mechanisms of FA-functionalized NPs, we first assessed their internalization in mixed human neuronal cell cultures composed of microglia, astrocytes, and neurons at a physiologically relevant ratio of 5:3:2. ICC analysis revealed robust uptake of FITC-FA-NPs across all three cell types, with microglia exhibiting markedly higher uptake rates than astrocytes and neurons (Fig. 3A). We next utilized murine organotypic brain slice cultures to preserve the three-dimensional cytoarchitecture of the brain, to evaluate spatiotemporal cellular uptake of FITC-FA-NPs. Following 1, 30, and 60 min of incubation, FITC-FA-NP uptake increased over time in all cell types. Co-localization of FITC-FA-NPs with the microglial marker IBA1 was detectable as early as 1 min post-incubation, indicating rapid interaction and uptake kinetics in microglia (Fig. 3B). Uptake-associated fluorescence was also observed in astrocytes and neurons, particularly at later time points. Given the cellular composition of organotypic brain tissue, these images are not intended for quantitative comparison between cell types. To dissect the mechanisms underlying FA-NP internalization, we pretreated neuronal cells with pharmacological inhibitors targeting distinct endocytic pathways: free folic acid (FA) to competitively block folate receptors (FOLR), Cytochalasin D (CytoD) to disrupt actin polymerization and phagocytosis, Rottlerin to inhibit macropinocytosis and non-clathrin pathways, and Dynasore to block dynamin-dependent endocytosis (Fig. 3C). We tested and utilized non-toxic molar concentrations of the inhibitors as previously described [52–54] (Fig. S2A and B). Administration of CytoD [10 μM] had no significant impact on ^{177}Lu-FA-NP uptake in any of the tested cell types, indicating that phagocytosis is not a major uptake route (Fig. 3D–F, Fig. S2A and B). In contrast, treatment with Rottlerin [6 μM] and Dynasore [10 μM] led to a significant reduction in ^{177}Lu-FA-NP uptake in all cell types, with the strongest effect observed in microglia ($p < 0.001$). Dose-dependent inhibition by both Rottlerin and Dynasore further confirmed their impact on microglial uptake (Fig. 3G and H). While treatment with free FA [1 mM] did not significantly reduce ^{177}Lu-FA-NP uptake in astrocytes and neurons, a significant decrease was observed in microglia ($p < 0.001$, Fig. 3D–F), indicating a FOLR-mediated endocytic uptake. We next pre-incubated HMC-3 microglial cells with free FA [1 mM] + Rottlerin [6 μM] or free FA [1 mM] + Dynasore [10 μM] for 30 min prior to ^{177}Lu-FA-NP administration to assess the combined inhibition of FOLR-mediated endocytosis. The combination of free FA and Rottlerin did not result in significant difference compared to treatment with rottlerin alone. In contrast, co-treatment of free FA + Dynasore revealed a significant reduction of ^{177}Lu-FA-NP uptake in microglia ($p < 0.001$) (Fig. 3I).

Collectively, these data indicate that FA-functionalized NPs are rapidly and predominantly internalized by microglia *via* dynamin- and FOLR-dependent endocytosis, while astrocytes and neurons display lower uptake. These findings underscore microglia as the principal cellular target of FA-NPs in the brain, offering insight into cell-specific delivery strategies for neurotherapeutics.

2.4. FA-NPs are rapidly internalized and retained in microglia for up to 96 h

To investigate the kinetics of microglial interaction with FA-NPs, we performed time-resolved uptake and retention studies using both ^{177}Lu-labeled or FITC-functionalized FA-NPs (Fig. 4A). Non-loaded carrier was utilized to avoid CytoD-induced alterations to basal trafficking pathways. ICC revealed a detectable internalization of FA-NPs (green) as early as 1 min post-incubation, with progressive cytoplasmic accumulation peaking between 30 and 60 min (Fig. 4B). Co-localization (yellow) with the microglial marker IBA1 confirmed cell-specific uptake, while DAPI-staining delineated nuclear morphology. The fluorescence images were intended to qualitatively visualize intracellular nanoparticle localization and retention rather than to provide direct quantitative uptake measurements. Quantitative uptake kinetics were therefore assessed separately using γ-Counter analysis of ^{177}Lu-labeled FA-NPs (Fig. 4C), which demonstrated rapid and significant NP uptake within the first minute (approx. 5 %), increasing steadily over time ($p < 0.001$). Uptake saturated at approximately 40 % after 60 min, with no further increase at 120 or 180 min, indicating that internalization reached a plateau within 1 h (Fig. 4D). To assess the intracellular retention time, we tracked NP localization using ICC with Lysotracker, revealing co-localized FITC-FA-NP signal within lysosomal compartments up to 96 h post-incubation (Fig. 4E). This was supported by γ-Counter measurements, which showed a gradual decrease in cell-associated radioactivity over time, accompanied by a corresponding increase in signal within the supernatant, consistent with NP efflux or

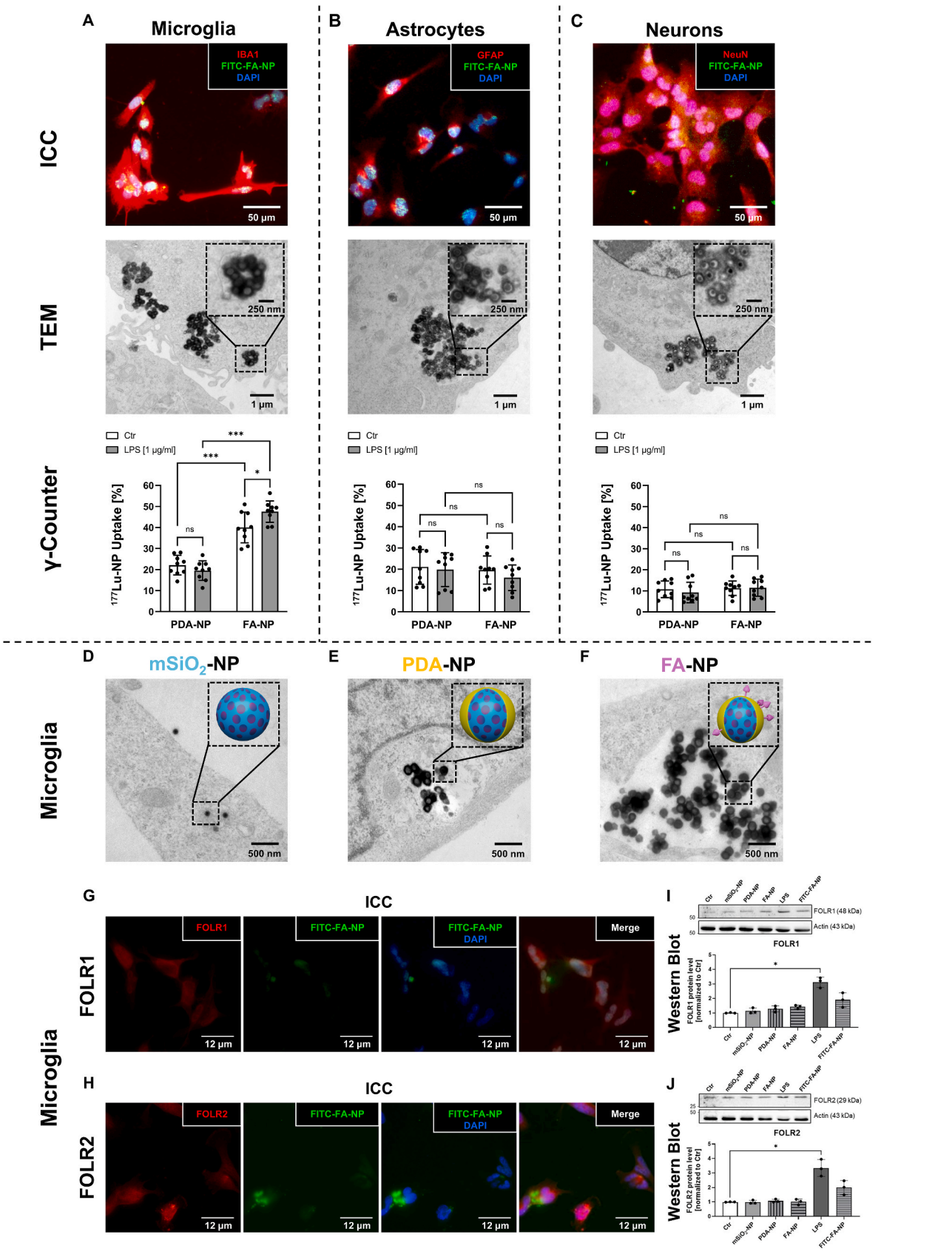

(caption on next page)

Fig. 2. Impact of NP surface functionalization on cellular uptake, intracellular localization, and distribution in neuronal cells. Cellular uptake rates using immunocytochemistry (ICC), transmission electron microscopy (TEM) and γ-Counter in **(A)** microglia (HMC-3), **(B)** astrocytes (U373), and **(C)** neurons (SY5Y). ICC co-staining of fluorophore-labeled FITC-FA-NP (green), DAPI (blue), and cell-specific markers IBA1 for microglia, GFAP for astrocytes, and NeuN for neurons (red) **(A-C top panel)**. Representative TEM images showed accumulated FA-NPs in the cytoplasm of all three cell lines captured after 1 h of NP incubation **(A-C middle panel)**. Decay-corrected quantitative cellular uptake rates of PDA-NP and FA-NP (control or 3 h LPS [1 μg/mL] treatment) were measured by γ-Counter using ^{177}Lu-labeled NPs [<0.01 Bq/cell] **(A-C bottom panel)**. Data are shown as means ± SD of 9 independent experiments with 2 technical replicates. A two-way ANOVA followed by multiple comparison tests and *Tukey's post-hoc test* was performed. Representative TEM images of $mSiO_2$-NPs **(D)**, PDA-NPs **(E)**, and FA-NPs **(F)** after 1 h of NP incubation in HMC-3 microglial cells. ICC analysis of HMC-3 microglial cells with FITC-FA-NPs, DAPI, FOLR1 **(G)**, and FOLR2 **(H)** antibodies. Western blot analysis of FOLR1 (~48 kDa) **(I)** and FOLR2 (~29 kDa) **(J)** with actin (~43 kDa) serving as loading control. Data are shown as means ± SD of 3 independent experiments with 3 technical replicates. A *Kruskal-Wallis test* followed by *Dunn's multiple comparisons test* was performed. *p < 0.05, **p < 0.01, ***p < 0.001; ns, not significant.

release (Fig. 4F).

Together, these data indicate that FA-NPs are rapidly and efficiently internalized by microglial cells, reaching maximum uptake within 60 min. Although intracellular levels decline over 96 h, a substantial fraction of FA-NPs is retained long-term, suggesting endolysosomal sequestration with partial release into the extracellular environment over time.

2.5. Intracellular pH triggers PDA shell degradation and cargo release from FA-NPs

To analyze the intracellular stability and release behavior of polydopamine (PDA)-coated folic acid-functionalized nanoparticles (FA-NPs), we investigated PDA shell degradation under acidic conditions and monitored NP-mediated delivery of DAPI cargo in microglial cells. Transmission electron microscopy (TEM) revealed that PDA shells remained largely intact in early endosomal compartments, while degradation was evident in larger vesicles corresponding to late endosomes (Fig. 5A). Morphological changes included thinning of the PDA layer (black vs. red arrows) and vesicle fusion events (marked with *), suggestive of dynamic endolysosomal processing (Fig. 5A). Quantification of PDA-shell thickness and surface under different pH conditions confirmed that acidic environments promote the degradation process. FA-NPs subjected to an experimental pH value of 5.0 displayed a significant degradation of the PDA-shell thickness and area compared to those maintained at physiological pH 7.4 ($p < 0.001$) (Fig. 5B and C, Fig. S3A and B). For these structural degradation analyses, the common FA-NP backbone was intentionally used, as the focus of the experiments was the PDA shell response rather than additional imaging or therapeutic modules. Similarly, intracellular PDA-shell degradation was evident by 48 h post-uptake in microglial cells, with further reduction at 96 h ($p < 0.001$), indicating progressive degradation over time (Fig. S3C and D). Notably, the PDA shells were not completely degraded at either time point, suggesting that a residual shell structure persists even after prolonged intracellular retention times. To assess functional cargo release capacity of FA-NPs, we encapsulated DAPI within FITC-labeled FA-NPs and monitored intracellular localization using immunocytochemistry. DAPI was used as a fluorescent surrogate cargo to enable direct visualization of time-dependent intracellular release kinetics. A time-dependent increase in cytosolic FITC signal was observed alongside progressive nuclear DAPI staining, starting as early as 5 min post-incubation and culminating in complete nuclear labeling by 60 min (Fig. 5D). Co-staining with Lysotracker identified acidic endolysosomal compartments, and partial overlap with FITC-positive nanoparticles (FITC-FA-NP[DAPI]) generated a merged yellow signal, supporting endolysosomal involvement in cargo release.

These data demonstrate that PDA-coated FA-NPs exhibit acid-sensitive degradation and support sustained intracellular release of cargo. Importantly, the observation that cargo release occurs despite incomplete PDA shell degradation supports the notion that full shell degradation is not required for effective delivery. This may point to a mechanism involving partial endosomal escape or localized shell disruption. Together, these findings highlight the utility of FA-NPs as a pH-responsive nanocarrier system capable of overcoming endolysosomal barriers for targeted intracellular delivery.

2.6. FA-NP encapsulated CytoD attenuate toxicity and selectively modulate microglial inflammatory response, migration and phagocytosis

Following our observation of efficient FA-NPs uptake by microglial cells, we investigated the downstream impact of NP exposure and CytoD delivery on microglial toxicity, oxidative stress, inflammatory response, and key microglial functions such as migration and phagocytosis. An exposure to bare $mSiO_2$-NPs, PDA-NPs, and FA-NPs for 1 h followed by washout revealed no acute toxicity at 24 h, as assessed by LDH release or cell viability after 24 h (Fig. 6A and B). However, at 96 h, the bare $mSiO_2$-NPs particles exhibited significantly increased LDH release and reduced microglial viability. In contrast, PDA and FA functionalization attenuated these effects, demonstrating a protective impact of surface modification. Free molecular CytoD [5 μM] induced significant cell death at both 24 h and 96 h post-incubation, while FA-NP-encapsulated CytoD (FA-NP[CytoD]) significantly reduced LDH release and cell death (Fig. 6A and B). Extended cytotoxicity analysis up to 120 h in microglia further revealed no significant differences in LDH release between vehicle-treated controls and PDA-NP- or FA-NP-treated cells, indicating preserved cellular viability despite prolonged nanoparticle exposure (Fig. S2G). Notably, the bare $mSiO_2$-NPs revealed decreased metabolic activity and increased ROS production in microglial cells at both 24 and 96 h (Fig. 6C and D). These findings indicate that under the prolonged exposure conditions used here, bare unmodified $mSiO_2$-NPs were not biologically inert in microglial cells, whereas PDA coating and FA functionalization markedly improved cellular compatibility. Interestingly, NPs with PDA coating and FA functionalization did not exhibit a significant reduction in metabolic activity compared to NaCl controls at both time points, indicating a protective effect of the functionalized NPs (Fig. 6C). Furthermore, functionalization with PDA and FA substantially reduced ROS production, suggesting a reduction in oxidative stress (Fig. 6D). In addition to increased toxicity, bare $mSiO_2$-NPs also elevated the expression of pro-inflammatory cytokines (IL-6, IL-1β, TNF, CCL2, and CCL5) and pro-apoptotic genes (BAX, CASP3, CASP8, and CASP9) at both 24 h and 96 h (Fig. 6E). PDA-coated and FA-functionalized NPs suppressed both inflammatory and apoptotic gene expression, highlighting the anti-inflammatory profile of functionalized particles and their capacity to reduce activation-associated toxicity (Fig. 6E). Given the reduced toxicity and inflammatory response observed with FA-NPs-encapsulated CytoD, we next assessed the impact of these NPs on key microglial functions such as migration and phagocytosis. Microglial migration was evaluated using a zone exclusion assay with time-lapse imaging over 48 h (Fig. 6F and G). FA-NPs significantly enhanced microglial migration compared to the NaCl control. However, the administration of molecular CytoD [5 μM] effectively inhibited migration. Encapsulation of CytoD within FA-NPs also led to a notable reduction in migration compared to FA-NPs alone, demonstrating that FA-NP[CytoD] effectively inhibit microglial mobility (Fig. 6F and G). With increasing concentrations of FA-NP-encapsulated CytoD [0–12.5 μg/mL], microglial cell migration decreased over a 48 h observation period (Fig. S4A). The administration of the endocytosis inhibitor Dynasore counteracted the inhibitory effect of CytoD on cell migration,

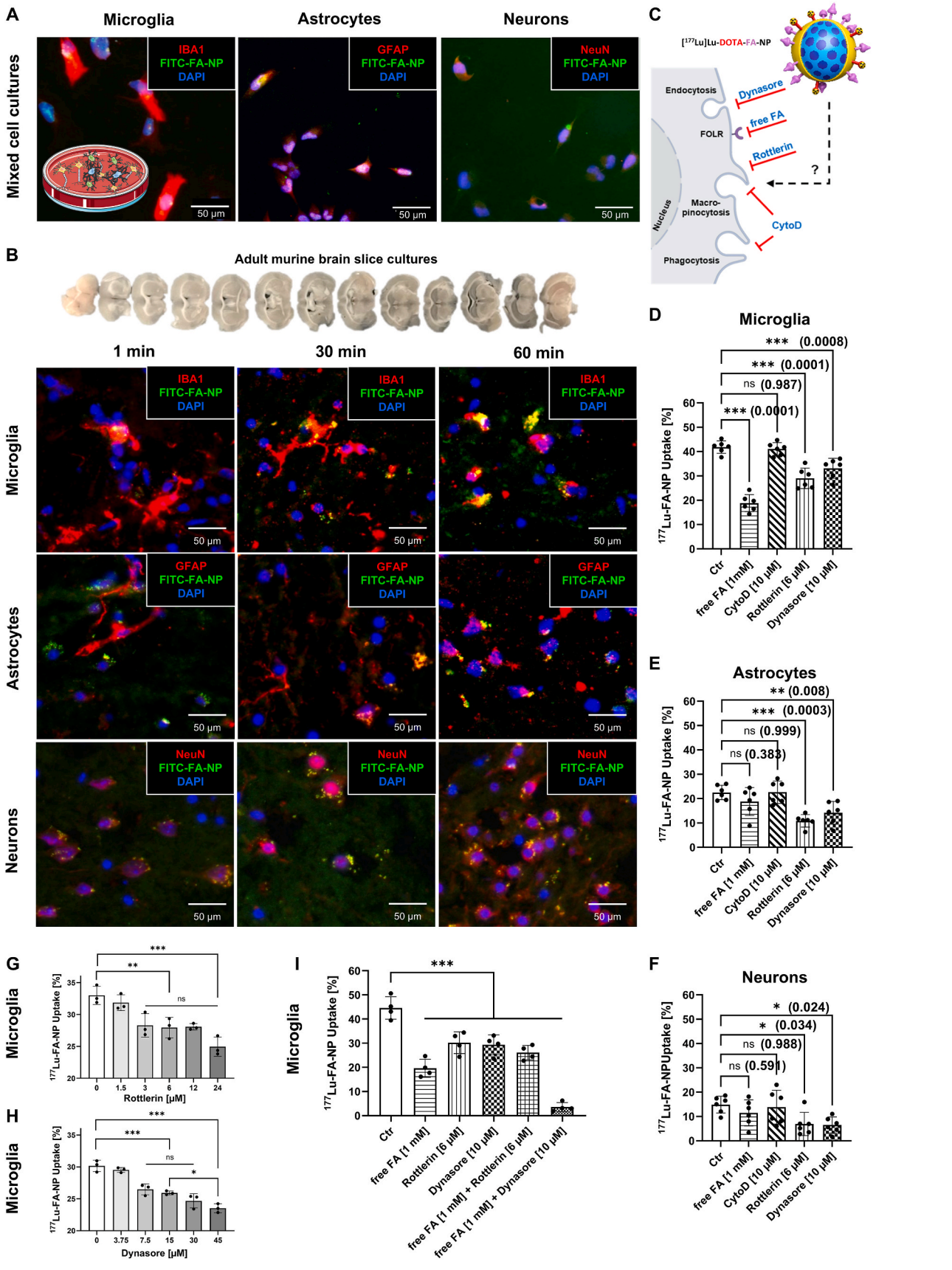

(caption on next page)

Fig. 3. Uptake mechanisms of FA-NPs in human mixed neuronal cell cultures and murine organotypic brain slice cultures. **(A)** Representative ICC images of FITC-FA-NPs in mixed human neuronal cell cultures 5:3:2 (microglia: astrocytes: neurons) with cell-specific markers for HMC-3 (IBA1), U373 (GFAP), and SY5Y (NeuN) after 1 h of FA-NP incubation. **(B)** Representative coronal murine brain slices (top panel) are 350 μm thick and preserve intact brain architecture. Immunohistochemical (IHC) analysis (bottom panel) of FITC-FA-NP uptake in adult murine organotypic brain slice cultures (12 μm sections) following 1 min, 30 min, and 60 min of FA-NP incubation. **(C)** Schematic overview of pharmacological inhibitors used to dissect uptake mechanisms of ^{177}Lu-FA-NPs (^{177}Lu-DOTA-FA-NP) without therapeutic cargo. **(D–F)** Decay-corrected γ-Counter analysis of cellular ^{177}Lu-FA-NP [<0.01 Bq/cell] uptake following 1 h of NP incubation in HMC-3, U373, and SY5Y cells treated for 30 min with free FA [1 mM], CytoD [10 μM], Rottlerin [6 μM], or Dynasore [10 μM]. Concentration-dependent quantitative ^{177}Lu-FA-NP [<0.01 Bq/cell] uptake in microglia was measured by γ-Counter after a FA-NP incubation time of 1 h using different molar concentrations of Rottlerin **(G)** and Dynasore **(H)** (treated 30 min prior to NP incubation). **(I)** Combined inhibition studies in microglia using co-treatment of free FA [1 mM] in combination with Rottlerin [6 μM] or Dynasore [10 μM] for 30 min prior to ^{177}Lu-FA-NP [<0.01 Bq/cell] incubation for 1 h. Data are shown as means ± SD of 3-6 independent experiments with 2-3 technical replicates. A one-way ANOVA followed by *Dunnett's multiple comparisons test* was performed. *$p < 0.05$, **$p < 0.01$, ***$p < 0.001$; ns, not significant.

further suggesting the endocytic uptake of the nanoparticles (Fig. S4B and C). To investigate phagocytic activity, microglial cells were incubated with pH-dependent coupled beads (pHrodo™) for 24 h and 48 h (Fig. 6H and I). CytoD significantly reduced phagocytosis at both time points, and NP-encapsulation of CytoD within FA-NPs similarly diminished microglial phagocytosis. In contrast, LPS [1 μg/mL] used as a positive control elicited the highest levels of phagocytosis, as expected (Fig. 6H and I).

In Summary, PDA coating and FA functionalization of NPs effectively reduce microglial toxicity, ROS production, and the inflammatory response. Furthermore, encapsulation of CytoD within FA-NPs preserves its functional ability to inhibit microglial migration and phagocytosis, while mitigating its cytotoxic effects. This suggests that functionalized FA-NPs may serve as a promising platform for modulating microglial activity in neuroinflammatory conditions.

2.7. FA-NP-encapsulated CytoD mitigate neuroinflammation following hypoxia-reoxygenation or focal brain injury

Acute hypoxic/ischemic and traumatic focal brain injuries represent the most common causes of neurological morbidity, characterized by rapid neuroinflammatory responses and secondary tissue damage. Based on the findings in Fig. 6, which showed that FA-NP[CytoD] retained the desired immunomodulatory activity of CytoD while markedly reducing the toxicity observed with free CytoD, we next investigated whether nanoparticle-mediated CytoD delivery could preserve therapeutic efficacy under injury-relevant conditions. Accordingly, the following experiments were designed to compare unloaded FA-NPs with FA-NP [CytoD] in two complementary acute brain injury models. Given the observed reduction of inflammatory and pro-apoptotic markers in microglial cells upon FA-NP-encapsulated CytoD treatment, we next evaluated its therapeutic potential in two *ex vivo* models of acute neurological injury: hypoxia-reoxygenation and focal thermocoagulation in adult murine brain slice cultures. In the hypoxia-reoxygenation model, organotypic adult murine brain slices (350 μm) were subjected to 30 min of hypoxia followed by reoxygenation for up to 96 h, with FA-NPs incubated for 1 h during the hypoxic period (Fig. 7A–C). Uptake rates of ^{177}Lu-labeled FA-NPs, measured *via* γ-counting, showed a significant increase in the hypoxic group at 24 h post-incubation ($p < 0.001$), while no significant difference in NP uptake was observed after 96 h in comparison to the normoxia group (Fig. 7D). As expected, hypoxia-reoxygenation injury led to elevated mRNA expression of pro-inflammatory cytokines IL-1β, IL-6, and TNF. While FA-NPs alone did not alter cytokine expression, treatment with FA-NP[CytoD] significantly suppressed all three cytokines at both 24 h and 96 h post-injury (Fig. 7E–G). To assess performance in the focal brain injury model, we employed a focal thermocoagulation injury model targeted to the motor cortex and adjacent subcortical structures, including the corpus callosum (Fig. 7H and I). Autoradiography showed lower FA-NP uptake in the ipsilesional hemisphere relative to the contralateral side, consistent with compromised local tissue integrity (Fig. 7J). γ-Counter quantification confirmed significantly greater FA-NP uptake in the contralateral hemisphere at 24 h ($p < 0.01$), which normalized by 96 h (Fig. 7K). Inflammatory gene expression was then assessed in ipsi- and contralateral hemispheres. In the ipsilesional tissue, FA-NP[CytoD] significantly reduced IL-1β, IL-6, and TNF mRNA expression at both 24 h and 96 h, compared to both NaCl and FA-NP controls ($p < 0.001$) (Fig. 7L–N). Similar anti-inflammatory effects were observed in the contralateral hemisphere, with significant reductions in IL-1β (24 h), IL-6 (96 h), and TNF (both time points).

Collectively, these findings demonstrate that FA-NP-encapsulated CytoD effectively suppresses inflammatory cytokine expression in models of ischemic-like and traumatic brain injury and support its potential as a promising nanotherapeutic candidate to be further evaluated in *in vivo* models of acute brain injury.

2.8. Systemic administration of FA-NPs enables brain delivery and cellular uptake with partial clearance by 24 h

To assess the *in vivo* biodistribution, BBB penetration capacity, and clearance profile of FA-NPs, mice were intravenously injected with ^{177}Lu-labeled (30 MBq) FITC-FA-NPs, followed by SPECT/CT imaging at 4 h and 24 h post-injection (Fig. 8A). SPECT/CT revealed an increased FA-NP accumulation in the brain parenchyma after 4 h following systemic administration. The signal intensity declined at 24 h, suggesting partial clearance or degradation of the nanoparticles over time (Fig. 8B). Post-mortem autoradiography (ARG) of serial coronal brain sections supported the imaging data, with widespread radiotracer accumulation observed at 24 h, and notably reduced signal at 120 h (Fig. 8C). Quantitative γ-Counter analysis confirmed this decline in nanoparticle retention, showing significantly higher counts per minute (CPM) at 24 h compared to 120 h ($p < 0.001$; Fig. 8D). To determine cellular distribution, immunohistochemistry (IHC) was performed using markers for microglia (IBA1), astrocytes (GFAP), and neurons (NeuN). At 24 h p.i., FITC-FA-NPs were clearly detectable in all three CNS cell types (Fig. 8E). These representative images were intended to qualitatively demonstrate parenchymal brain accumulation and cellular association of FA-NPs in the healthy brain rather than to provide a quantitative comparison of cell type-specific uptake *in vivo*. By 120 h p.i., FITC signal was visibly diminished across all cell types, consistent with the SPECT/CT, ARG, and γ-Counter data (Fig. 8F).

Together, these results confirm that FA-NPs can efficiently cross the BBB and reach key neural cell populations *in vivo* as early as 4 h post-injection. The signal decline after 120 h suggests clearance or degradation, supporting the potential for transient CNS delivery without long-term accumulation - an important feature for translational therapeutic applications.

3. Discussion

Modulating prolonged or dysregulated microglial activation after acute brain injuries, including stroke, trauma, and hypoxic insults, holds strong therapeutic promise for mitigating secondary damage. However, systemic delivery of immunomodulatory drugs to the brain remains severely limited by the BBB, which prevents most therapeutics from accessing parenchymal targets. To address this challenge, we developed a multifunctional theranostic PDA-coated, FA-functionalized $mSiO_2$-NP platform, designed to facilitate parenchymal brain accumulation,

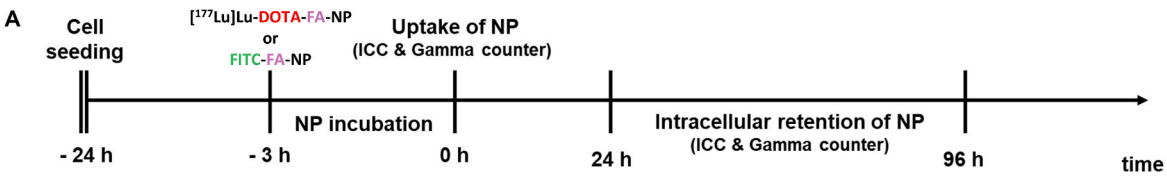

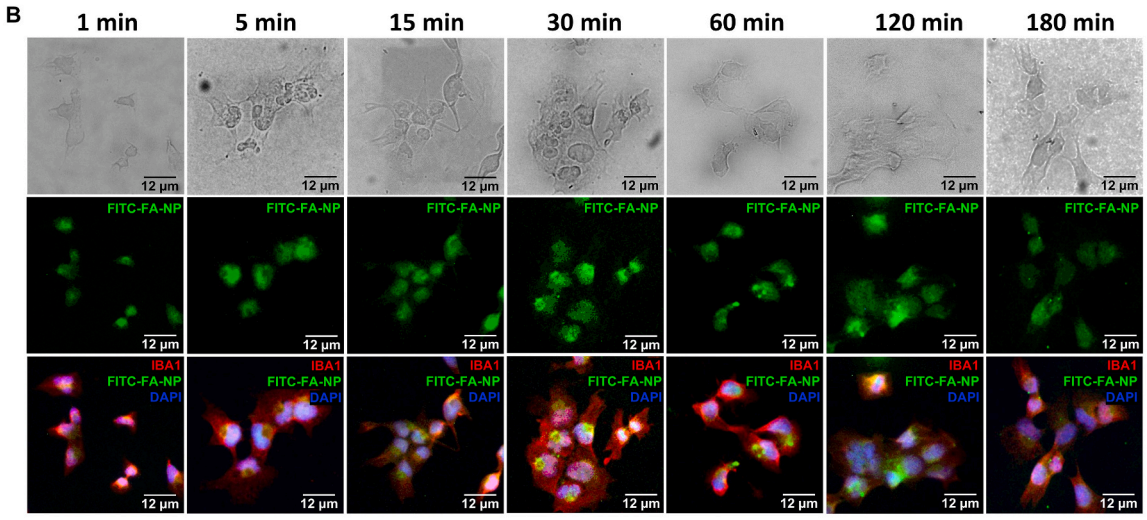

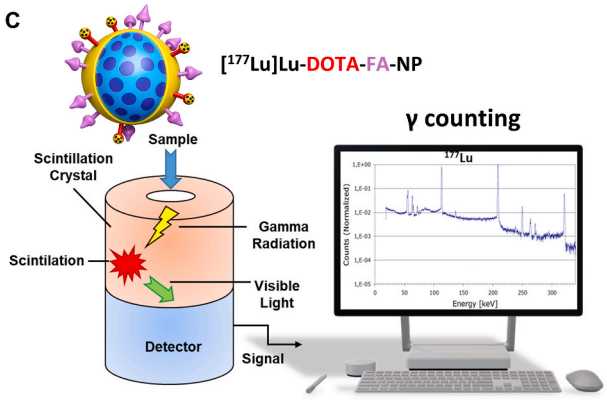

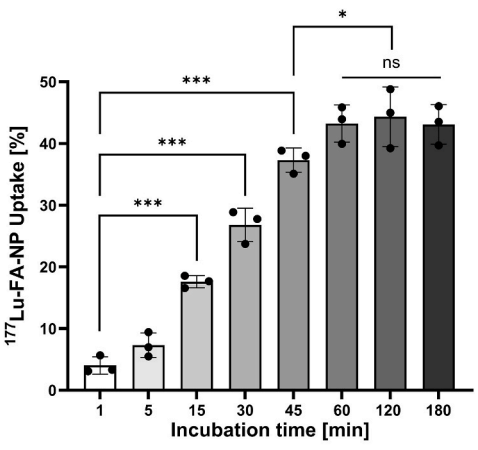

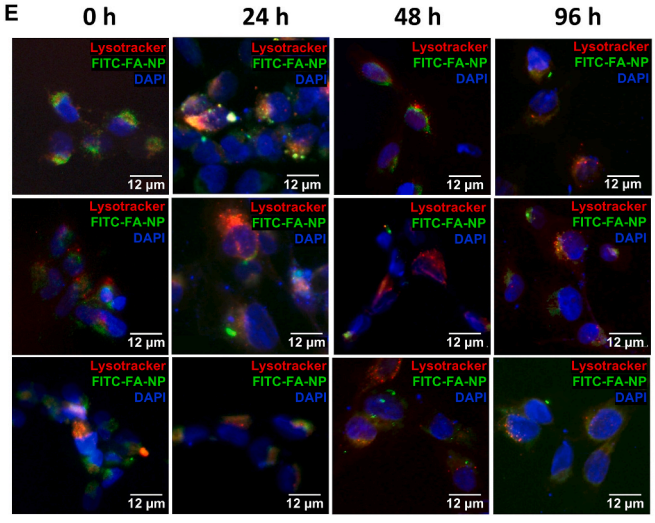

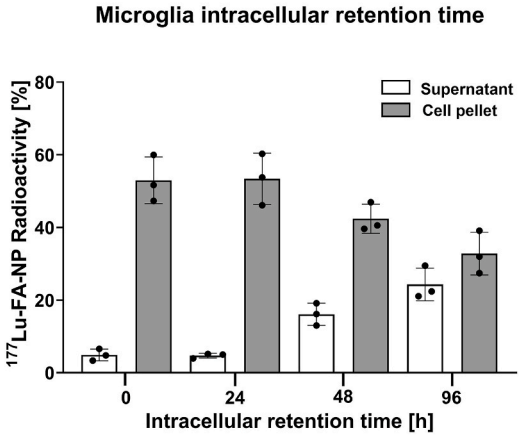

(caption on next page)

Fig. 4. Time-dependent uptake and intracellular retention time of FA-NPs in microglia. **(A)** Schematic overview of the experimental workflow for time-resolved uptake and retention assays using FITC- or ^{177}Lu-labeled FA-NPs. **(B)** Time-dependent uptake of FITC-FA-NPs (green) in microglia using ICC staining (DAPI (blue) and IBA1 (red)). **(C)** Diagram of the γ-Counter setup used to measure ^{177}Lu-FA-NP (^{177}Lu-DOTA-FA-NP) accumulation in cell lysates and supernatants. **(D)** Decay-corrected quantitative γ-Counter uptake rates of ^{177}Lu-labeled FA-NPs [<0.01 Bq/cell] up to 3 h of NP incubation. **(E)** Time-dependent retention measurements using ICC analysis with FITC-FA-NPs (green), DAPI (blue), and Lysotracker (red) up to 96 h of intracellular retention. **(F)** Decay-corrected quantitative γ-Counter measurements with ^{177}Lu-labeled FA-NPs [<0.01 Bq/cell] up to 96 h of intracellular retention. Data are shown as means ± SD of 3 independent experiments with 3 technical replicates. A one-way ANOVA followed by *Dunnett's multiple comparisons test* was performed. *p < 0.05, **p < 0.01, ***p < 0.001; ns, not significant. (For interpretation of the references to color in this figure legend, the reader is referred to the Web version of this article.)

microglial targeting, controlled intracellular drug release, and imaging-guided tracking. A key advantage of this system is its modular architecture. Rather than representing separate NP systems, the fluorescently-, radiolabeled, and drug-loaded variants used in this study were derived from the same FA-NP backbone and served complementary mechanistic, imaging, and therapeutic functions. This design enabled cross-validation across experimental modalities, while the same carrier backbone can be flexibly adapted with fluorescent or radiometal-based modules to monitor uptake, biodistribution, clearance, multimodal imaging, or serve as a payload-agnostic platform for future therapeutic cargos. Such versatility enhances both translational relevance and overall novelty.

$mSiO_2$-NPs possess unique structural and physicochemical properties that confer chemical stability, tunable surface functionality, and excellent biocompatibility, establishing them as promising carriers for the targeted delivery of theranostic payloads [55–57]. Their mesoporous architecture facilitates drug encapsulation while reducing hemolytic activity compared to nonporous silica NPs, attributed to reduced silanol density [58,59] (Fig. 1A). Key parameters such as particle size and surface chemistry critically influence NP behavior in the organism [60]. While Napierska et al., reported that $mSiO_2$-NPs larger than 100 nm exhibit minimal endothelial toxicity, particles smaller than 50 nm can induce significant necrotic cell death [61]. Although particles smaller than 100 nm have been proposed as efficient carriers for organ-targeted delivery [62], other studies suggest that appropriate surface functionalization can facilitate effective BBB translocation independent of size [63]. Our FA-NPs, composed of a ~110 nm silica core with a ~29 nm PDA coating, exhibited hydrodynamic diameters of 220–260 nm and a low polydispersity index (PDI <0.15), confirming uniformity and stable modification (Fig. 1C–E). The surface zeta potentials, ranging from −28.5 to −41.2 mV, are within the optimal range for stable nano-dispersions and BBB compatibility [64] (Fig. 1B). Anionic surface charges have been shown to better preserve BBB integrity and facilitate brain delivery compared to cationic particles [65,66]. Consistently, Zhang et al. and Chen et al. reported enhanced BBB penetration and brain accumulation of negatively charged $mSiO_2$-NPs, with permeability influenced by both surface charge and particle size [65,67,68]. Moreover, PDA-coated $mSiO_2$-NPs, but not uncoated silica particles, were recently shown to cross the BBB *in vivo* [47]. Our data align with these findings and support the conclusion that surface charge, controlled size, and functionalization collectively enable effective BBB permeability (Fig. 1B–E, Fig. 8). However, the relatively high hydrodynamic diameters (Fig. 1C–E) *in sera* might lead to enhanced accumulation of the particles in lung as previously reported and therefore require further investigation [60,69,70]. Mechanistically, our results revealed that FA-NP are internalized by microglia *via* FOLR-mediated, clathrin- and dynamin-dependent endocytosis (Fig. 2D–J; Fig. 3C–I). Uptake was significantly reduced by Dynasore and free FA, but unaffected by CytoD, ruling out phagocytosis and macropinocytosis. The significant uptake reduction by free FA in microglia, but not in astrocytes or neurons, highlights cell-specific folate receptor engagement. The nanoparticle size (~140 nm) further supports this pathway, as particles <200 nm preferentially undergo clathrin-mediated uptake [71], while caveolae-mediated internalization typically dominates above 500 nm and is less relevant in brain tissue due to low caveolin-1 expression in microglia [72]. While FOLR1 has been described preferentially upregulated by choroid plexus ependymal cells, oligodendrocyte precursor cells and midbrain dopamine progenitor cells [73–76], FOLR2 has been found upregulated in embryonic meningeal border-associated macrophages and microglia [77]. More recent studies using spatial transcriptomics analysis reported FOLR2 upregulation in human adult microglia, suggesting a potential shift in receptor expression with maturation or disease context [78–80]. Supporting these transcriptomic observations, our own IHC and Western blot analyses confirmed the presence of both FOLR1 and FOLR2 proteins in human microglial cells, with a marked increase in abundance following LPS stimulation (Fig. 2). This LPS-induced upregulation may further enhance the selective uptake of FA-functionalized nanoparticles under inflammatory conditions. The preferential uptake we observed may therefore reflect a previously underappreciated translational window for targeting microglia in the adult brain *via* folate-linked delivery (Fig. 2A–C, Fig. 3B). Rapid intracellular accumulation in microglial populations within 1 min of exposure, particularly in acute neuroinflammatory hotspots, highlights the spatial and temporal precision of this delivery platform (Figs. 3B and 4B–D).

Once internalized, FA-NPs accumulated in endolysosomal compartments with extended retention over 96 h, accompanied by gradual exocytosis (Fig. 2A–C, Fig. 4E&F, Fig. 5A). The PDA coating conferred pH-responsiveness, as shown by time- and pH-dependent degradation of the polymer shell (Fig. 5A–C) and release of the encapsulated nuclear dye DAPI (Fig. 5D). TEM and ICC data (Fig. 5) suggest that full shell degradation is not required for cargo delivery, underscoring the utility of PDA for temporally controlled, intracellular drug release. Such behavior is critical in inflammatory environments characterized by acidic pH [81]. To achieve a sustained and effective therapeutic effect, FA-NPs must enable prolonged intracellular retention and controlled release of their payload. This typically requires successful escape from endolysosomal compartments, allowing cytoplasmic access to the cargo [82–84]. Our data suggest that PDA-coated NPs remain partially intact intracellularly over extended periods, as evidenced by the gradual degradation of the PDA shell observed up to 96 h post-incubation (Fig. 5A–C). This slow degradation supports a model of progressive intracellular release. Although we did not directly investigate the mechanism of endosomal escape, previous studies have proposed several possibilities for nanoparticle-mediated cytoplasmic delivery, including endosomal fusion, osmotic lysis *via* the proton sponge effect, vesicular rupture, and pH-triggered disassembly [85,86]. We also observed partially degraded FA-NPs in cell culture supernatants, indicating that a fraction of the nanoparticles is eventually exocytosed. Whether these extracellular particles can be taken up again by neighboring cells in multicellular systems or tissues remains unclear. Recent studies further suggest that inorganic nanoparticle composition itself may influence intracellular processing and exocytotic clearance mechanisms in microglia, potentially through altered vesicular trafficking and extracellular vesicle biogenesis [87]. While we observed prolonged intracellular retention of FA-NPs, our *in vitro* experiments did not reveal major impairments in microglial migration or phagocytic activity following nanoparticle exposure (Fig. 6). However, mechanistic analyses will be required to determine whether the mesoporous silica-based FA-NP composition and degradable PDA-coating directly contributes to altered microglial clearance behavior. Likewise, the fate of these particles *in vivo*, particularly their renal and hepatobiliary clearance dynamics, represents an important open question. Understanding the mechanisms governing systemic elimination and potential recirculation will be essential for advancing this platform toward safe and clinically

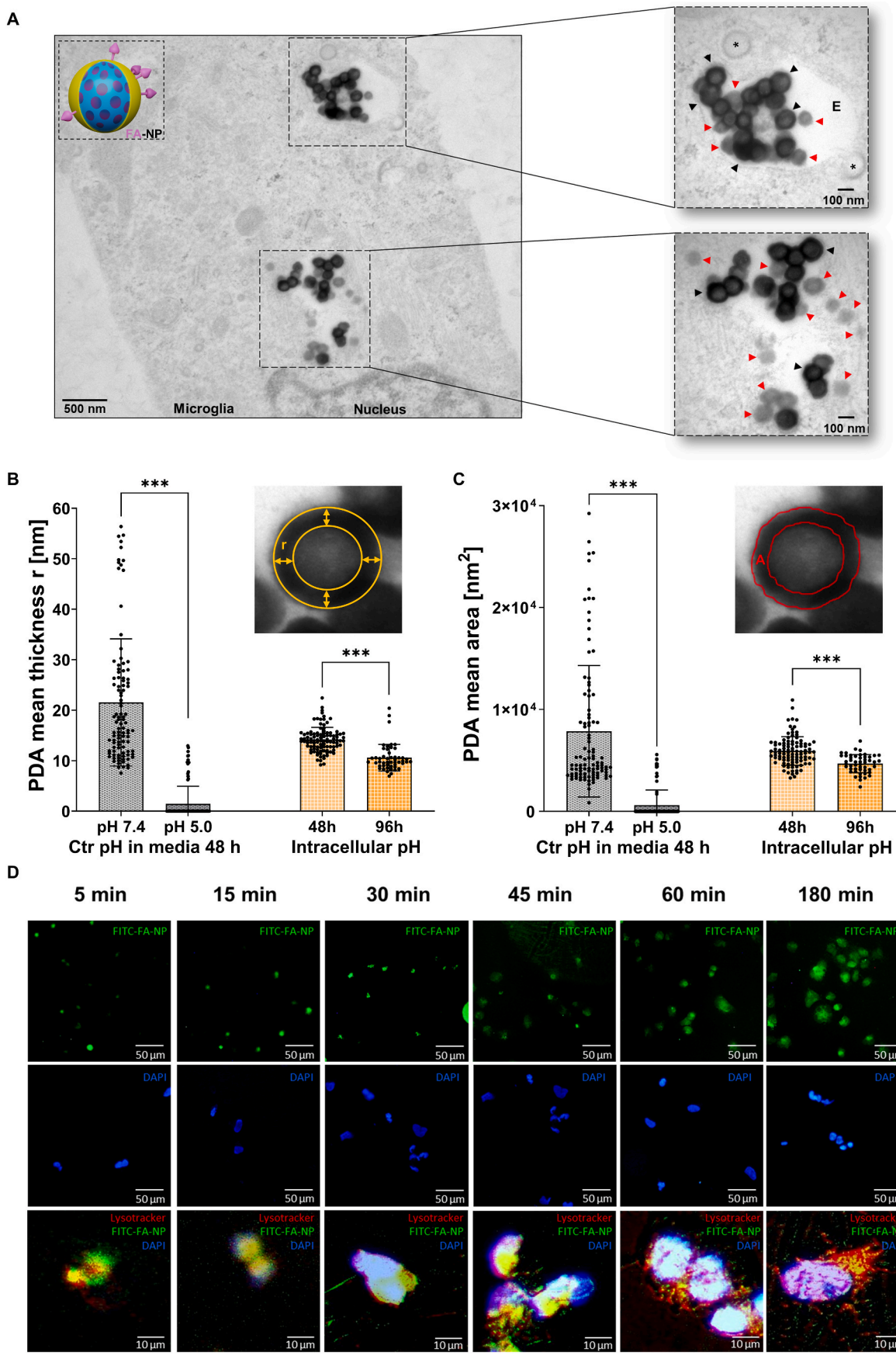

(caption on next page)

Fig. 5. pH-dependent PDA-shell degradation and intracellular drug release of FA-NPs in microglia. **(A)** Representative TEM images of FA-NPs internalized in HMC-3 microglial cells, showing influence on PDA coating in early and late endosomes (E) (red arrow = decreased PDA shell; black arrow = mostly intact PDA shell). PDA mean thickness r (mean of four different shell locations) **(B)** and PDA mean area **(C)** of FA-NPs incubated in media (48 h at pH 7.4 or 5.0, respectively) and after an intracellular retention time of 48 h or 96 h in HMC-3 microglial cells were measured using ImageJ. **(D)** Time-dependent cargo release in ICC staining of DAPI-loaded FITC-FA-NPs in microglia, co-stained with a Lysotracker. Bars represent means ± SD. 50-100 FA-NPs per condition were analyzed. A two-tailed *t*-test followed by *Welch's test* was performed. *$p < 0.05$, **$p < 0.01$, ***$p < 0.001$; ns, not significant. (For interpretation of the references to color in this figure legend, the reader is referred to the Web version of this article.)

viable applications.

Surface functionalization is known to improve the biocompatibility of $mSiO_2$-NPs by reducing nonspecific protein adsorption, cytotoxicity and hemolytic activity [60,88–90]. Additionally, NP-surface modifications with PEG or PDA have been shown to reduce uptake by the liver, spleen, and lungs, thereby prolonging systemic circulation and enhancing *in vivo* distribution profiles [65,91–93]. Although silica-based nanoparticles are frequently described as biocompatible, their safety profile is highly context-dependent and influenced by particle size, porosity, surface chemistry, concentration, cell type, intracellular retention, and exposure duration. Our findings indicate that prolonged exposure of microglial cells to bare unmodified $mSiO_2$-NPs can induce measurable stress responses, whereas PDA and FA functionalization markedly mitigated these effects. Although extended LDH release analyses up to 120 h in microglia did not reveal significant toxicity for PDA-NPs or FA-NPs compared to vehicle-treated controls, the delayed intracellular fate of residual bare $mSiO_2$ cores following prolonged intracellular retention remains incompletely understood and should be addressed in future studies focusing on long-term vesicular processing, exocytotic clearance, and potential late-onset microglial stress responses. These observations further emphasize that rational surface engineering is critical for optimizing the CNS compatibility of silica-based nanocarriers (Fig. 6). Our PDA- and FA-coated NPs exhibited reduced toxicity, ROS production, and cytokine expression compared to bare $mSiO_2$-NPs (Fig. 6A–E). Encapsulation of CytoD within FA-NPs preserved its immunosuppressive effects, reducing microglial migration, phagocytosis, and cytokine production, while minimizing toxicity associated with free CytoD (Fig. 6F–I).

In both hypoxia-reoxygenation and focal thermocoagulation injury models in adult murine brain slices, FA-NP[CytoD] treatment significantly suppressed IL-1β, IL-6, and TNF expression up to 96 h (Fig. 7). These results underscore the therapeutic potential of our system in modulating acute neuroinflammation. Notably, FA-NPs alone had no detectable immunosuppressive effects, confirming that therapeutic activity was cargo-dependent. This is consistent with previous findings that nanoparticle encapsulation enhances CytoD efficacy and safety *in vivo* [94]. Overall, these findings indicate that encapsulated CytoD retains its biological activity while targeted delivery circumvents systemic toxicity [27], a key challenge that has historically limited its translational potential.

Importantly, while many nanoparticle formulations face translational hurdles due to poor CNS delivery or off-target toxicity, our FA-NP[CytoD] system addresses both. Its modular design allows for tuning of surface chemistry, ligand density, and drug payload, while dual radiolabeling with ^{68}Ga and ^{177}Lu supports both diagnostic imaging and therapeutic tracking, key requirements for precision medicine. However, several limitations remain. Organotypic brain slices do not fully replicate the vascular and immune dynamics of the intact CNS, and LPS-induced microglial activation captures only part of the complex neuroinflammatory response after acute brain injury. LPS stimulation was therefore intentionally used as a controlled and reproducible activation paradigm for mechanistic uptake studies rather than as a comprehensive disease model of acute brain injury. Moreover, while intracellular parenchymal accumulation of FA-NPs was observed *in vivo* following systemic administration, the precise mechanisms governing BBB trafficking and neurovascular transport remain to be elucidated. Additionally, CytoD's actin-modulating effects may differentially affect cell types and require longer-term evaluation *in vivo*. Future work should validate this platform in animal models of stroke or traumatic injury, assess long-term safety and efficacy, and explore disease-specific payloads tailored to microglial phenotypes. In this context, extended *in vivo* histopathological analyses and peripheral organ toxicity assessments will be important to further evaluate the long-term biocompatibility and safety profile of FA-NPs following systemic administration. Additionally, optimization of dosing regimens, surface ligand density, and clearance kinetics will be essential for clinical translation.

In summary, we present a multifunctional theranostic FA-NP[CytoD] platform that combines brain delivery, microglial targeting, controlled intracellular drug release, and real-time imaging capability. By integrating diagnosis and therapy within a single nanocarrier architecture, this strategy offers promising translational potential for acute brain injuries and broader neuroinflammatory disorders. These findings warrant further *in vivo* validation to advance this approach toward clinical translation.

4. Experimental section

4.1. Nanoparticle synthesis and functionalization

Template-assisted Sol-Gel Synthesis of $mSiO_2$-NPs: For the synthesis, an experimental description [89] was followed with minor modifications as previously described [51]. Initially, 0.365 g [1.0 mmol] CTAB was dissolved in 100 mL of water under magnetically stirring at an elevated temperature of 80 °C, followed by the addition of 0.350 g NH_4F. Afterwards, 1.80 mL TEOS was added dropwise to the clear solution with a speed of 1 mL/min and the mixture was stirred for another 2.5 h at 80 °C. After cooling down, the bluish-shimmering, white dispersion was centrifuged to collect $mSiO_2$ NPs. Subsequently, NPs were re-dispersed in acetone/diluted HCl and sonicated for 30 min to ensure the removal of any residuals of CTAB. Finally, additional washing steps of NPs with EtOH to remove any excess of released surfactant and silica were performed. Drying 24 h at ambient temperature, prepared the $mSiO_2$-NPs for further characterization studies.

Synthesis of Polydopamine-coated $mSiO_2$-NPs: $mSiO_2$-NPs were coated with polydopamine (PDA) by polymerizing dopamine under alkaline conditions. Therefore, a protocol [95] was followed with minor modifications as previously described [51]. Firstly, 0.040 g of $mSiO_2$-NPs were dispersed in 60 mL of TRIS buffer (pH 8.5) [10 mM], and then 0.110 g dopamine hydrochloride was dissolved in the dispersion. The pH was adjusted again to pH 8.5 and the reaction was magnetically stirred for 24 h in the dark being exposed to oxygen. After adding dopamine hydrochloride, the reaction mixture immediately started to change its color turning from pale-yellow over yellowish orange to dark brown. The dark brown core-shell NPs were collected *via* centrifugation and washed several times with EtOH and water to remove any excess of polydopamine. Drying 24 h at ambient temperature, prepared the PDA-NPs for further characterization studies.

Conjugation of Folic Acid on PDA-coated NPs: Folic acid was conjugated with its carboxy functions to residual NH_2-groups of PDA-coated NPs *via* carbodiimide coupling reaction [96] with minor modifications as previously described [51]. For this approach, 0.130 g FA was dissolved in 100 mL acetone, 0.060 g of DCC was added and the reaction mixture was allowed to stir magnetically continuously at ambient temperature in the dark for 5 h. Afterwards, 0.035 g of NHS was added and the reaction mixture stirred at ambient temperature for further 24 h (in the dark). After pre-activation of the carboxy functions of FA with DCC

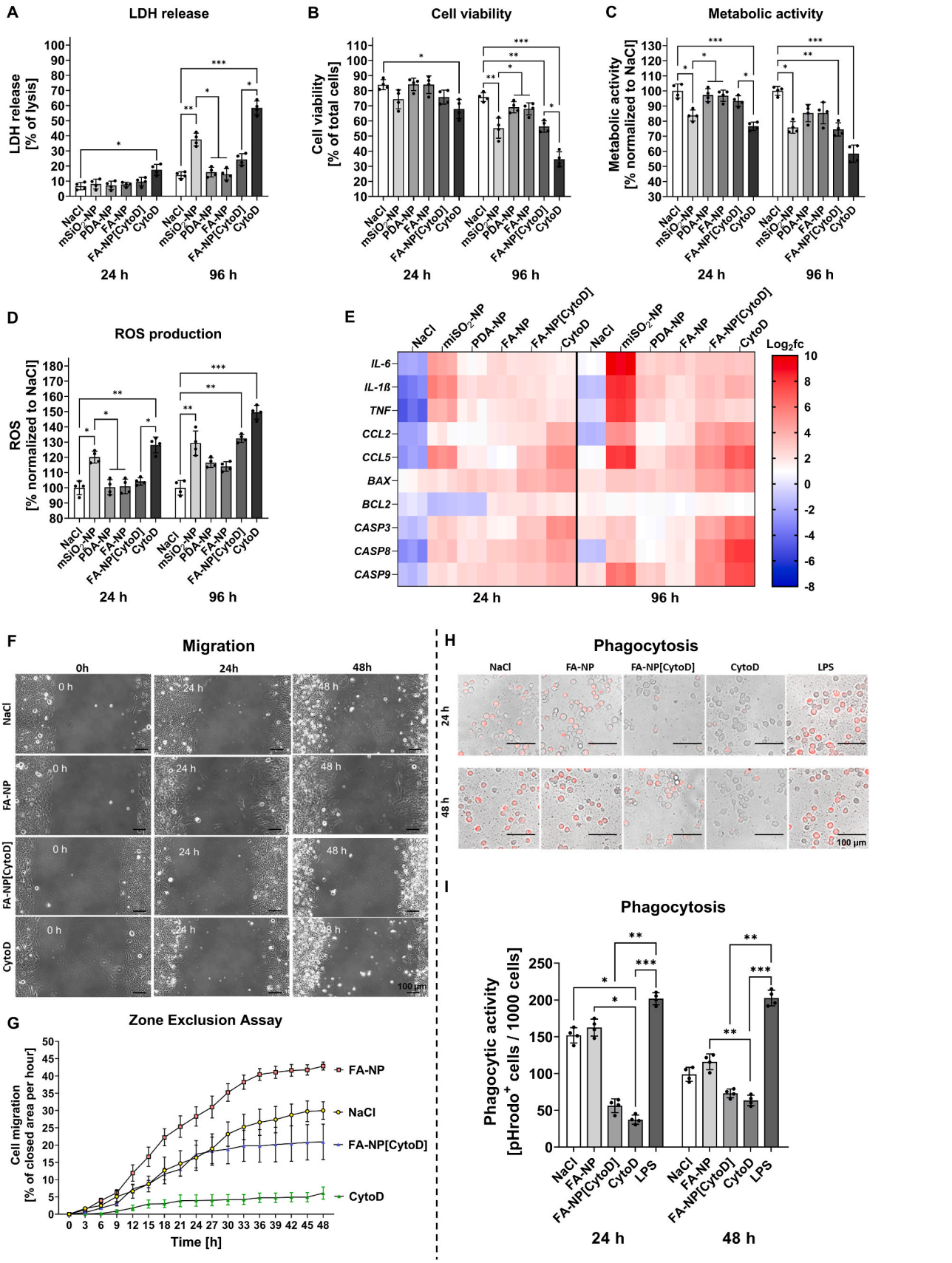

(caption on next page)

Fig. 6. Impact of PDA coating, FA functionalization, and CytoD encapsulation on toxicity, ROS production, inflammatory response, phagocytosis, and migration of human microglial cells. Cellular toxicity and inflammatory response were measured both at 24 h and 96 h post-incubation (incubation time 1 h) for bare $mSiO_2$-NPs, PDA-NPs, FA-NPs, FA-NPs-encapsulated CytoD (FA-NP[CytoD]), molecular CytoD [5 μM] and the corresponding NaCl control. **(A)** LDH release, **(B)** cell viability using cell counter, **(C)** metabolic activity, **(D)** ROS production and **(E)** impact on inflammatory cytokines and pro-apoptotic genes. Data are shown as means ± SD of 3-4 independent experiments with 3 technical replicates. A *Kruskal-Wallis test* followed by *Dunn's multiple comparisons test* was performed. Migration ability was assessed using a zone exclusion assay. **(F)** Representative images of microglial HMC-3 migration over a period of 48 h after stimulation. The images shown in Fig. 6F are representative snapshots selected from a 48 h time-lapse recording. **(G)** Quantification of HMC-3 migration treated either with NaCl (control), FA-NP [6.25 μg/mL], FA-NP[CytoD] [6.25 μg/mL] and molecular CytoD [5 μM] up to 48 h. Data are presented as means ± SEM of 6 individual experiments with 2 technical replicates in each experiment. **(H)** Representative images of phagocytic activity are shown. Phagocytic activity of microglial HMC-3 cells using pHrodo™ Red E. coli Bioparticles™ after 1 h of treatmet with either NaCl (control), FA-NP [6.25 μg/mL], FA-NP[CytoD] [6.25 μg/mL], molecular CytoD [5 μM] and LPS (positive control, 1 μg/mL) was assessed at 24 and 48 h. **(I)** Quantification of phagocytic activity. pHrodo™ Red E. coli Bioparticles™ positive cells per 1000 counted cells were quantified in each experiment. Data are shown as means ± SD of 4 independent experiments with 3 technical replicates. A *Kruskal-Wallis test* followed by *Dunn's multiple comparisons test* was performed. *$p < 0.05$, **$p < 0.01$, ***$p < 0.001$; ns, not significant.

and NHS, 0.105 g of PDA-NPs were re-dispersed in the reaction mixture carefully and the dispersion was stirred at ambient temperature in the absence of light for 48 h. Finally, the FA-NPs were separated from the supernatant *via* centrifugation and washed additional times with EtOH until any excess of FA was removed and the supernatant was colorless. Drying at ambient temperature for 24 h made the FA-NPs eligible for further characterizations.

Chelator/Dye Attachment: To covalently attach DOTA as a chelator for radiometal labeling, as previously described [51] 10 mg of either FA-NP or PDA-NP were re-dispered in 2 mL of a (1:1) Na_2CO_3-buffer/ultrapure water solution (Merck, Darmstadt, Germany). 2.9 mg of p–SCN–Bn-DOTA (Macrocyclics, Plano, USA) was dissolved in 2 mL Na_2CO_3-buffer (pH 9) and added dropwise to NP dispersion. The reaction mixture was heated up to 37 °C and stirred overnight. After cooling down, the NPs were collected *via* centrifugation (4000 rpm) and washed one time with Na_2CO_3-buffer and one time with ultrapure water before drying at ambient temperature. To covalently bind FITC, 400 μL of an aqueous FITC solution [1 mg/mL] (Merck, Darmstadt, Germany) was added to 1 mL of an aqueous FA-NP or PDA-NP dispersion [1.5 mg/mL] in metal free water. The mixture was stirred 6-8 h in the dark. To remove unbound FITC the mixture was washed several times with ethanol/-water (1:1) and centrifuged at around 4500 x g for 10 min and the supernatant was removed. The washing procedure was repeated up to six times until supernatant is colorless.

Drug Loading: Drug loading of Cytochalasin D (CytoD) or 4′,6-Diamidino-2-phenylindol (DAPI) into mesoporous NPs was achieved *via* a diffusion effect. To 250 μL of an aqueous NP dispersion [1.5 mg/mL], 0.5 μL [5 mg/mL EtOH] CytoD (Merck, Darmstadt, Germany) or 5 μL [0.02 mg/mL H_2O] DAPI (Roth, Karlsruhe, Germany) was added, and the mixture was magnetically stirred for 24 h at RT. For Purification the mixture was centrifuged (4000 rpm for 5 min) and washed three times with ultrapure water (Merck, Darmstadt, Germany) while the supernatant was collected.

Drug Release: To determine the pH-dependent PDA-shell degradation, NPs were incubated extracellular in media for 48 h at pH values of 7.4 or 5.0. Furthermore, to evaluate the intracellular PDA degradation FA-NPs were incubated for 1 h in microglial HMC-3 cells and were assessed after retention times of 48 h or 96 h. TEM images were taken, and ImageJ was used to analyze the PDA mean thickness r (four different points for each NP) and the PDA mean area in all four conditions.

4.2. Nanoparticle characterization

Zeta Potential: The zeta potential values (ζ-potential) of the bare and surface engineered NPs were measured on a Zetasizer Nano ZS (Malvern Panalytical, Malvern, UK) in aqueous solution in triplicate.

Fourier-Transform Infrared spectroscopy: To evaluate the successful NP synthesis, modification and functionalization, Fourier-Transform Infrared (FT-IR) spectra for the detection of functional groups on the synthesized and functionalized NPs were recorded as previously shown [51] on a Spectrum 400 (PerkinElmer, Waltham, USA) with Universal ATR sampling accessory in the range of 4000 to 400 cm^{-1}.

Transmission Electron Microscopy: For morphology, size and shape analysis the NPs were were fixed in 3 % glutaraldehyde in 0.1 M Soerensen's phosphate buffer (Merck, Darmstadt, Germany) and embedded in 2.5 % low-melting agarose (Sigma, Steinheim, Germany). After post-fixing with 1 % OsO_4 (Roth, Karlsruhe, Germany) in 25 mM sucrose buffer (Merck, Darmstadt, Germany) the samples were dehydrated by ascending ethanol series (30, 50, 70, 90 and 3 times 100 %) for 10 min each. Dehydrated samples were incubated in propylene oxide for 30 min, then in a mixture of Epon resin (Serva, Heidelberg, Germany) and propylene oxide (Science Services, Munich, Germany) (1:1) for 1h and finally in pure Epon for 1h. Samples were embedded in fresh Epon and polymerized at 90 °C for 2h. Ultrathin sections (~90 nm) were stained with 0.5 % uranyl acetate and 1 % lead citrate (both EMS, Munich, Germany) to enhance contrast. Samples were examined using a transmission electron microscope (Zeiss Leo906, Oberkochen, Germany) operating at an acceleration voltage of 60 kV.

Nanoparticle Tracking Analysis: Size distribution and polydispersity of the NPs were determined using nanoparticle tracking analysis (NTA) measurements on a LM10SH (NanoSight, Malvern, United Kingdom), equipped with a sample chamber with a 532 nm laser. The captured videos were analyzed by the NTA 2.0 image analysis software (NanoSight, Malvern, UK). The mode and mean size and SD values were obtained by the NTA software.

4.3. Radiochemistry

Radiolabeling: Radiolabeling was carried out as previously described [51]. To 1.5 mg of p–SCN–Bn-DOTA-modified FA-NP or PDA-NP 1 mL metal free ultrapure water (Merck, Darmstadt, Germany) was added and the mixture was sonicated for 5 min at 30 °C. 40-250 μL [1.5 mg/mL] of that NP dispersion were transferred to a 2 mL glass reaction vial, using an aqueous ammonium acetate solution [3 M] as buffer. In case of ^{68}Ga-labeling, up to 110 μL [^{68}Ga]$GaCl_3$ (up to 500 MBq) were added. The radionuclide was supplied by a ^{68}Ge/^{68}Ga-generator (iThemba, Cape Town, South Africa) using 0.6 M HCl as eluent. In case of ^{177}Lu-labeling, up to 1 GBq $^{177}LuCl_3$ (volume <50 μL) in 0.04 M HCl (ITM, Munich, Germany) were added. The reaction took place at 90 °C for 10 min. Radiochemical yields (>98 %) and radiochemical purities (>98 %) of ^{68}Ga- and ^{177}Lu-labeled NPs were determined by radio-TLC (Elysia-Raytest, Straubenhardt, Germany) with citrate buffer (pH 5.0) as mobile and iTLC-SG strips (Agilent, Santa Clara, USA) as stationary phase.

In vitro Stability: Stability of ^{68}Ga and ^{177}Lu-labeled NPs was determined as previously described [51], by incubating the radiolabeled compound in PBS (pH 7.4) or human sera (1:9) at 37 °C. Aliquots thereof were analyzed at specified time points (for ^{68}Ga at: 15, 45, 60, 90, 120 and 180 min; for ^{177}Lu at: 0, 1, 2, 4, 24, 48, 72, 96 and 120 h) by radio-TLC regarding the present fraction of labeled NPs. Human sera were obtained from three healthy adult female and three healthy adult male donors. For assessment of nanoparticle stability under CSF-mimicking conditions, FA-NPs were incubated in aCSF at 37 °C and pH 7.4 for up to 24 h aCSF was prepared based on the standard

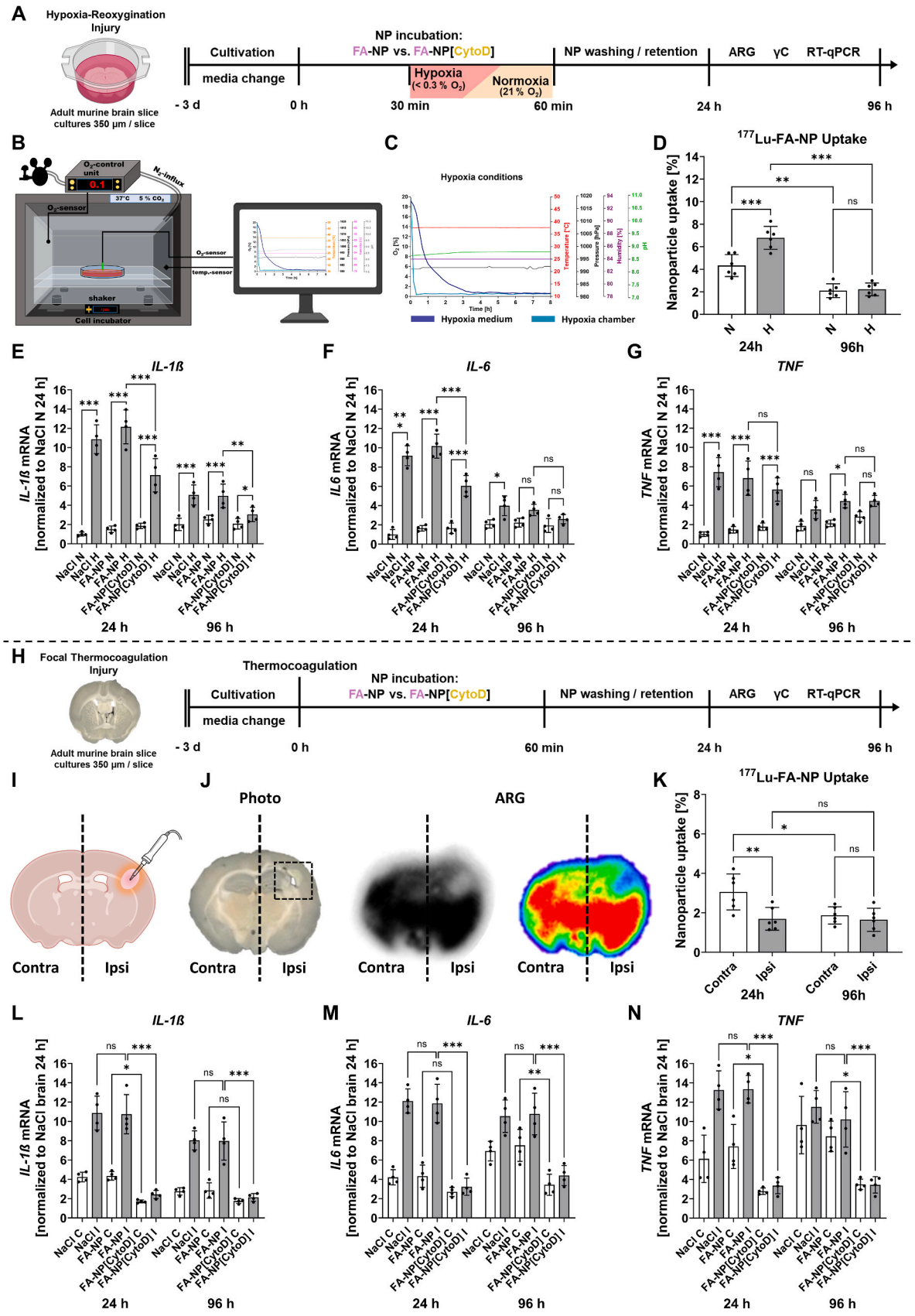

(caption on next page)

Fig. 7. Impact of FA-NP-encapsulated CytoD on proinflammatory cytokine transcript levels in organotypic adult murine brain slice cultures after hypoxia-reoxygenation or focal thermocoagulation injury. **(A)** Protocol of hypoxia-reoxygenation injury in organotypic adult murine brain slice cultures (350 μm sections). **(B)** Schematic illustration of hypoxia-chamber with **(C)** hypoxia conditions. **(D)** Time-dependent (24 h or 96 h post-NP incubation) γ-Counter uptake rates of ^{177}Lu-labeled FA-NPs [<0.01 Bq/cell]) in organotypic adult murine brain slice cultures are presented (N = normoxia; H = hypoxia). mRNA levels of IL-1β **(E)**, IL-6 **(F)**, and TNF **(G)** were assessed 24 h or 96 h post-hypoxia/normoxia after NP incubation. Brain slices were incubated with FA-NP or FA-NP[CytoD] [6.25 μg/mL] for 1 h in both injury models. **(H)** Protocol of focal thermocoagulation injury in organotypic adult murine brain slice cultures (350 μm/slice). **(I)** A schematic illustration of cortical/subcortical focal thermocoagulation injury. **(J)** Representative picture and autoradiography (ARG) of a coronal organotypic adult murine brain slice (350 μm sections) after focal thermocoagulation and incubation with ^{177}Lu-labeled FA-NPs [<0.01 Bq/cell]. **(K)** Time-dependent (24 h or 96 h post-NP incubation of 1 h) γ-Counter uptake rates of ^{177}Lu-labeled FA-NPs [<0.01 Bq/cell] in ipsi- (I) and contra-lesional (C) brain hemispheres. mRNA levels of IL-1β **(L)**, IL-6 **(M),** and TNF **(N)** were assessed 24 h or 96 h after focal brain injury. Intergroup differences were tested by two-way ANOVA followed by *Tukey's post-hoc test* (multiple comparisons). Bars represent means ± SD of 4-6 individual experiments with 3 technical replicates in each experiment. *p < 0.05, **p < 0.01, ***p < 0.001; ns, not significant.

composition routinely used in the work group. The final aCSF solution contained 125 mM NaCl (Millipore), 25 mM $NaHCO_3$ (Sigma), 2.5 mM KCl (Millipore), 1.25 mM NaH_2PO_4 (Millipore), 1 mM $MgCl_2{\cdot}6H_2O$ (Millipore), 2 mM $CaCl_2$ (Sigma), and 25 mM glucose (Millipore). $MgCl_2{\cdot}6H_2O$ was prepared separately as a 1 M stock solution and added freshly prior to use. A second stock solution containing 25 mM glucose and 2 mM $CaCl_2$ was prepared separately to avoid precipitation. For preparation of aCSF, the respective stock solutions were diluted in ultrapure water to the final concentrations indicated above. The solution was adjusted to pH 7.4 and maintained at 37 °C prior to experimental use.

Partition Coefficient: As previously described [51], to a 1:1 water/-hexane mixture, 2 MBq of ^{177}Lu-labeled NPs were added. The mixture was vigorously vortexed for at least 10 min. 0.1 mL of each layer was pipetted into a test tube and the radioactivity was measured using a Wizard^2 gamma counter (PerkinElmer, Waltham, USA). The measurement was carried out in triplicate. The partition coefficient (P) was calculated as a ratio of counts in the hexane phase to counts in the PBS phase (background corrected) and logarithmized to yield the logP.

4.4. Cells

Human HMC-3 microglial cell line (ATCC: CRL-3304), were kindly provided by Prof. Cordian Beyer (Institute of Neuroanatomy, Medical Faculty, RWTH Aachen University). Human glioblastoma astrocytoma cell line U-373 MG (Uppsala) (ECACC 08061901) were kindly provided by Dr. Brunkhorst (Department of Neurology, Medical Faculty, RWTH Aachen University). Human neuroblastoma cell line SH-SY5Y was politely provided by Dr. Aaron Voigt (Department of Neurology, Medical Faculty, RWTH Aachen University). HMC-3, U-373 and SY5Y cells were cultivated in Dulbecco's modified Eagle's medium (DMEM, Pan Biotech, Aidenbach, Germany) supplemented with 10 % fetal bovine serum (FBS, Pan Biotech, Aidenbach, Germany) and 0.5 % penicillin/streptomycin (P06-07100 (P/S, Pan Biotech, Aidenbach, Germany)). All cells were maintained in a humidified incubator at 37 °C and 5 % CO_2. HMC-3 cells were split every 2 days at approximately 75 % confluency by trypsinization (Trypsin/EDTA, Pan Biotech, Aidenbach, Germany). Regular PCR controls against gene markers of cell types used in our laboratory ensured the purity of the cell lines. One day prior to experiments the cells were detached by trypsinization with subsequent centrifugation (400 g, 5 min, room temperature (RT)). The cell pellet was resuspended in DMEM, 5 % FBS, 0.5 % P/S (all Pan Biotech, Aidenbach, Germany) and seeded in 6-well dishes for experiments and on coverslips for ICC.

4.5. Cell uptake

For all *in vitro* uptake experiments, PDA-NPs or FA-NPs were applied at a concentration of 6.25 μg/mL in cell culture medium. This concentration was selected based on preliminary optimization to ensure robust cellular uptake while maintaining cell viability.

Transmission Electron Microscopy: Microglia (HMC-3), Astrocyte (U373) and Neuron (SY5Y) cell lines were cultured in 6-well plates with a seeding density of 750x10^3 cells/well. To assess the nanoparticle uptake, individual well was treated with a cold FA-NP formulation diluted in 3 mL culture media and incubated for 1 h at 37 °C. After washing with PBS, the cells were fixed in 3 % glutaraldehyde in 0.1 M Soerensen's phosphate buffer (Merck, Darmstadt, Germany), scratched off the plate, pelleted *via* centrifugation and embedded in 2.5 % low-melting agarose (Sigma, Steinheim, Germany). Samples were further processed for transmission electron microscopy as already described.

Gamma Counter: To assess the quantitative nanoparticle uptake, as previously described [51] individual well was treated with different ^{177}Lu-labeled nanoparticle formulations of either functionalized with folic acid or control in a <0.01 Bq/cell concentration diluted in 3 mL culture media and incubated for 1 h at 37 °C. After washing with PBS, the cells were trypsinized, collected in a γ-Counter test tube, and their radioactivity was measured using a γ-Counter (Wizard^2, PerkinElmer, Waltham, USA) with a protocol for ^{177}Lu calibration. Efficiency corrected cell total activities were then expressed as counts per minute. Each experiment was performed three times with three technical replicates respectively. To determine the percentage of NP incorporation into the cells, the exact total initial activity of NP was calculated by counting 1 mL of a 1:10 dilution after the same incubation time. Background radiation was determined with 1 mL of culture medium. The percentage of NP incorporation was calculated using the following formula:

$$NP_I[\%] = \frac{A_{cells} - A_{Background}}{A_0} \times 100$$

where NP_I is the incorporation percentage and A_{cells}, $A_{Background}$, A_0 are the disintegrations per minute, registered for the cells, background radiation, and the dilution-corrected initial activity, respectively.

To determine the relative NP uptake of each condition, the γ-Counter measured uptake was calculated as percentage from the initial ^{177}Lu-labeled nanoparticle-culture media solution. For uptake studies with inhibitor treatment, cells were pretreated for 30 min with free FA [1 mM], CytoD [10 μM], Dynasore [10 μM], Rottlerin [6 μM], or a combination of free FA [1 mM] + Dynasore [10 μM] or free FA [1 mM] + Rottlerin [6 μM] prior to nanoparticle addition for an incubation period of 1 h at 37 °C.

4.6. Western blot

Western blot (WB) analysis was performed as previously described [97,98]. After incubating microglial HMC-3 cells with nanoparticles, cells were lyzed ice-cold radioimmunoprecipitation assay buffer (RIPA) supplemented with phosphatase and proteinase inhibitors (cOmplete, #1187358001, Roche, Basel, Switzerland). 20 μg of protein was loaded onto the SDS-PAGE gel and separated. After the transfer onto the PVDF membrane (Roche, Basel, Switzerland) and blocking with 5 % skim milk (#T145.3, Roth, Karlsruhe, Germany) in tris-buffered saline containing 0.05 % Tween20 (#8076.4, Roth, Karlsruhe, Germany), we incubated the membrane with the primary antibody in corresponding concentrations (Table 1). Following the incubation with the secondary horseradish-conjugated antibody, we visualized the results using ECL™ Plus Kit (Thermo Fisher Scientific, Waltham, MA, USA). β-Actin served as a loading control. Densitometric analysis was performed using ImageJ

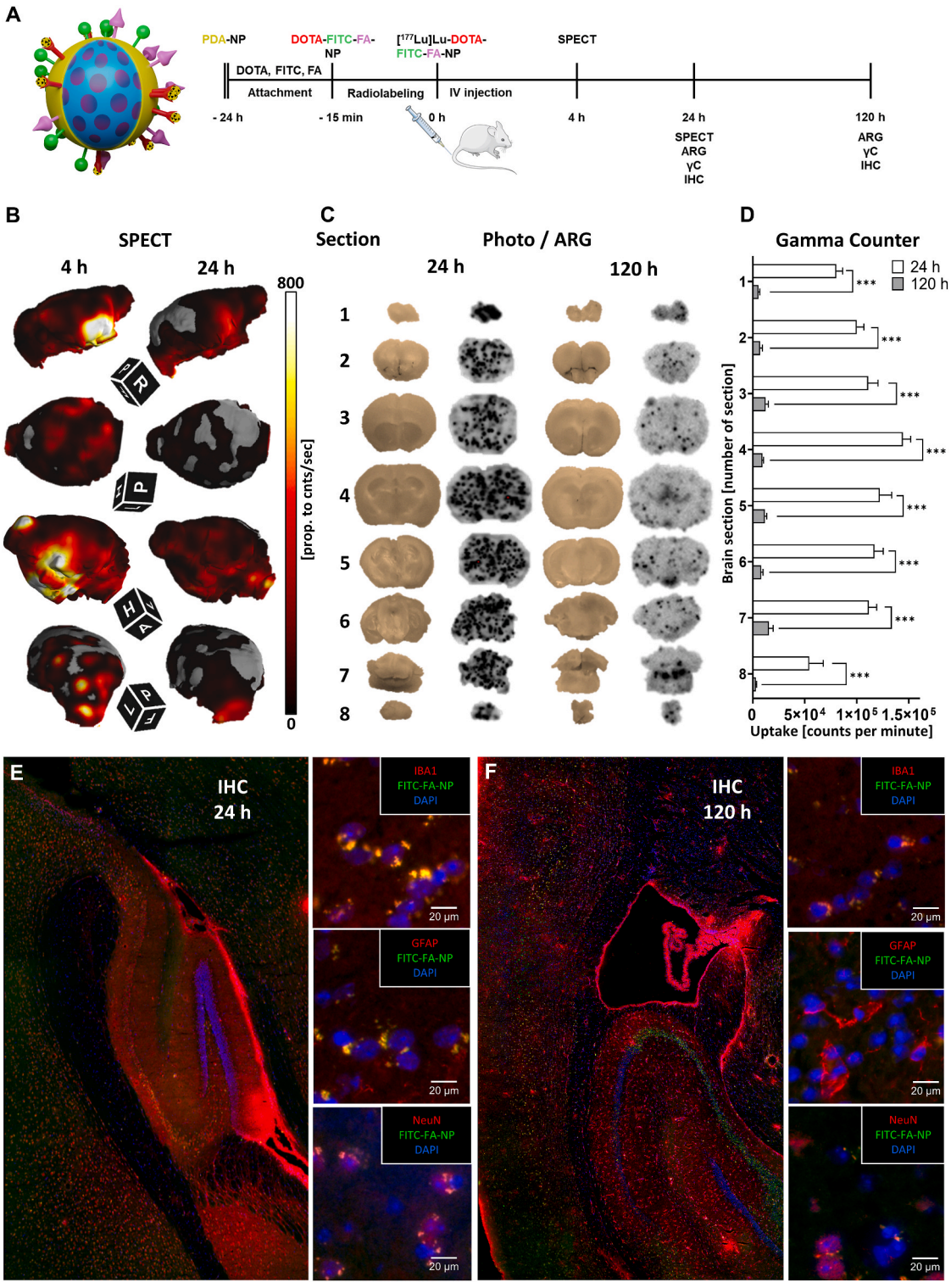

Fig. 8. Time-dependent *in vivo* biodistribution, quantification, and retention of FA-NPs in murine brains. **(A)** Schematic experimental procedure: ^{177}Lu-labeled and FITC-functionalized FA-NPs (30 MBq) were intravenously injected into mice. SPECT/CT imaging was performed at 4 h (n = 3) or 24 h (n = 3) post-injection (p.i.), followed by post-mortem (p.m.) ARG, γ-Counter quantification, and IHC analysis at 24 h and 120 h. **(B)** SPECT/CT images at 4 h or 24 h p.i. show the distribution of ^{177}Lu-labeled FA-NPs in the brain. All 3D-rendered brain SPECT/CT images were displayed with identical SPECT intensity limits of 0-800 proportional to counts/sec using the same Hot color scale. **(C)** ARG of 2 mm coronal brain sections at 24 h or 120 h post-injection. **(D)** Decay-corrected quantitative γ-Counter analysis, represented as counts per minute (CPM) for individual brain sections, shows the FA-NP retention over time at 24h or 120 h. A one-way ANOVA followed by multiple comparison tests and *Tukey's post-hoc test* was performed. IHC analysis of brain sections at 24 h **(E)** or 120 h **(F)** p.i. demonstrates the localization of FITC-FA-NPs within the brain using markers for microglia (IBA1), astrocytes (GFAP), and neurons (NeuN). The displayed IHC images represent qualitative examples of intracellular nanoparticle association within CNS cell populations and were intended as complementary histological validation of the quantitative SPECT/CT, autoradiography, and γ-counter biodistribution analyses rather than for region-specific neuroanatomical comparison. The magnified (40×) images are taken from the cortex. *$p < 0.05$, **$p < 0.01$, ***$p < 0.001$; ns, not significant. (For interpretation of the references to color in this figure legend, the reader is referred to the Web version of this article.)

Table 1
List of antibodies used for Western Blot.

Antibody	Company	Order number	Host	Dilution
FolR1	Cloud-Clone Corp., TX, USA	PAF460Ra01	Rat	1:500
FolR2	Abcam, Cambridge, United Kingdom	Ab103998	Rabbit	1:500
Rabbit IgG	GE, Healthcare, Chicago, IL, USA	NA934	Goat	1:5000
Mouse IgG	GE Healthcare, Chicago, IL, USA	NXA931	Goat	1:5000
β-Actin	Abcam, Cambridge, United Kingdom	Ab3280	Mouse	1:1000

(NIH, Bethesda, MD, United States).

4.7. Immunocytochemistry (ICC)

ICC analysis was performed according to established protocol [97,98]. Cells were seeded to Poly-L-lysine covered cover slips. After stimulation, cover slips were fixed with 4 % formaldehyde in phosphate buffered saline (PBS) and permeabilized with 0.2 % Triton X-100. Subsequently the slides were blocked with Immunofluorescence Blocking Buffer (1 % BSA, 2 % FBS in PBS) and incubated with the primary antibody overnight at 4 °C. The secondary antibody was incubated for 1 h at room temperature. Negative controls were incubated with only PBS buffer overnight. For the time-dependent intracellular retention time and drug release experiment of FITC-FA-NPs in microglia, LysoTracker™ Red DND-99 (Thermo Fisher Scientific, Waltham, MA, USA) was added 1 h before the end of nanoparticle incubation time. Cell nuclei were stained with 4′,6-Diamidino-2-phenylindol (DAPI) (Roth, Karlsruhe, Germany). Stainings were evaluated using a Leica fluorescence microscope (Leica, Wetzlar, Germany). List of antibodies used for immunocytochemistry is given in Table 2.

4.8. Fluorescence activated cell sorting

HMC-3 cells were incubated with Rottlerin [6 μM], Dynasore [10 μM], CytoD [10 μM], CytoD-loaded FA-NPs [6.25 μg/mL] and H_2O_2 (0.1 %) for 1 h at 37 °C. After 1 h of incubation time with the mentioned treatments, medium was changed, and cells were maintained for 24 h. After 24 h, cells were harvested by taking the supernatant and incubating the remaining cells for 5 min with trypsin (at 37 °C). HMC-3 cells were centrifuged and stained with Annexin V (Alexa Fluor 647) and PI and analyzed with FACSCanto™ II (BD Bioscience, Erembodegem, Belgium).

4.9. Cell viability

Cell viability was measured as previously described [97], using a lactate-dehydrogenase (LDH) assay according to the manufacturer's protocol (LDH, CytoTox 96® Non-Radioactive Cytotoxicity Assay, Promega, Walldorf, Germany). The release of stable cytosolic LDH into the extracellular space occurs during late apoptosis or necrosis of cells. Therefore, the amount of released LDH was measured in the supernatant at 490-520 nm using a microplate reader (Tecan, Männedorf, Switzerland). Cells treated with lysis solution served as an internal positive control, as previously shown [97,99]. The percentage of released LDH was determined by referring to the positive control, which was referred to as 100 % of possible LDH release. The findings were validated utilizing Trypan Blue staining (#T8154, Sigma-Aldrich, St. Louis, USA). Here, viable cells were counted by an automated cell counter (Roche Innovatis Cedex XS, Basel, Switzerland).

Table 2
List of antibodies used for immunocytochemistry and immunohistochemistry.

Antibody	Company	Order number	Host	Dilution
IBA1	Wako Chemicals, Neuss, Germany	019-19741	rabbit	1:1000
GFAP	Millipore, Burlington, MA, USA	MAB3402	mouse	1:500
NeuN	Millipore, Burlington, MA, USA	MAB377	mouse	1:1000
goat anti-mouse IgG Alexa Fluor 594	Invitrogen, Karlsruhe, Germany	A11032	goat	1:500
goat anti-rabbit IgG Alexa Fluor 594	Invitrogen, Karlsruhe, Germany	A11012	goat	1:500

4.10. Metabolic activity

Cell metabolism was measured as previously described [97], by CellTiter-Blue assay according to the manufacturer's protocol (CellTiter-Blue assay, Promega, Walldorf, Germany). The reduction of blue resazurin to pink, fluorescent resorufin requires an intact mitochondrial respiratory chain and can be observed only in metabolically active cells. The reduction of resazurin was observed in viable cells at 590 nm by a microplate reader (Tecan GmbH, Männedorf, Switzerland) as previously described [97,100].

4.11. ROS assay

The ROS assay was performed according to the manufacturer's protocol and as previously described [97]. In brief, 5 μM CellROXTM (C10444, Thermo Fisher Scientific, Waltham, MA, United States) reagent was added to the medium. After 30 min of incubation at 37 °C the supernatant was removed, and the cells were washed three times with PBS. Fluorescence was measured at an excitation wavelength of 488 nm and emission wavelength of 525 nm as previously described [97].

4.12. Reverse transcription quantitative PCR

Gene expression analysis was performed as previously described [97] with human microglial HMC-3 cells. After dissolving and homogenizing cells in PegGold (PeqLab #30-2010, Erlangen, Germany) total RNA was extracted using peqGold RNA TriFast as previously described [97,98]. Complementary DNA was synthesized using an iScript™ cDNA Synthesis Kit (Bio-Rad Laboratories, CA, United States) and random hexanucleotide primers (Invitrogen, Karlsruhe, Germany) using 1 μg of total RNA according to the manufacturer's protocol. Triplicates of every sample were transferred by a pipetting robot (Corbett CAS-1200, Qiagen, Hilden, Germany) to Rotor-Gene strip reaction tubes (I1402-0400, StarLab, Hamburg, Germany) and RT-qPCR analysis was performed using the Rotor-Gene Q device (Qiagen, Hilden, Germany). RNase free H_2O (Merck, 64293, Darmstadt, Germany) served as no template control (NTC) and primer efficiencies were calculated using the Pfaffl method [101]. The target genes and housekeeping gene (glyceraldehyde-3-phosphate dehydrogenase, GAPDH) were measured at cycle threshold (Ct values), and relative quantification was calculated by the 11Ct method using the qbase + software (Biogazelle, Belgium). The following forward (fwd) and reverse (rev) primers were used (50 - > 3 0): GAPDH (fwd: CCT GCA CCA CCA ACT GCT TA, rev: GGCCATCCACAGTCTTCTCAG), IL-6 (fwd: ACTCACCTCTTCAGAACGAATTG, rev: CCATCTTTGGAAGGTTCAGGTTG), IL-1β (fwd: CTT CGA GGC ACA AGG CAC AA, rev: TTC ACT GGC GAG CTC AGG TA), TNF (fwd: CCTCTCTCTAATCAGCCCTCTG, rev: GAGGACCTGGGAGTAGATGAG), CCL2 (fwd: CAGCCAGATGCAATCAATGCC, rev: TGGAATCCTGAACCCACTTCT), CCL5 (fwd: CCAGCAGTCGTCTTTGTCAC, rev: CTCTGGGTTGGCACACACTT), BAX (fwd: CCCGAGAGGTCTTTTTCCGAG, rev: CCAGCCCATGATGGTTCTGAT), BCL2 (fwd: GGTGGGGTCATGTGTGTGG, rev: CGGTTCAGGTACTCAGTCATCC), CASP 3 (fwd: CATGGAAGCGAATCAATGGACT, rev: CTGTACCAGACCGAGATGTCA), CASP8 (fwd: TTTCTGCCTACAGGTTCCACT,

rev: CCTCAATTCTGATCTGCTCACTT), CASP9 (fwd: CTTCGTTTCTGCGAACTAACAGG, rev: GCACCACTGGGGTAAGGTTT).

4.13. Zone exclusion/cell migration assay

Zone exclusion assay was performed like previously described by Arik et al. [97]. For 48 h the migration of HMC-3 cells was observed. One day prior to the experiments 70 µL of 500,000 cells/mL were seeded into 2 well culture-inserts (80209, Ibidi GmbH, Germany). After 24 h the medium was changed, and cells were left to incubate for 1 h with different conditions. Treatment conditions included drug-unloaded FA-NP [6.25 µg/mL], FA-NP-encapsulated Cytochalasin D (#C2618, Sigma-Aldrich, Taufkirchen, Germany) [6.25 µg/mL] and molecular CytoD [5 µM] dissolved in DMEM with 5 % FBS, 0.5 % P/S. Medium with NaCl and only 5 % FBS and 0.5 % P/S served as vehicle control. Afterwards, the inlets were removed, thus creating a 500 µm sized gap between both cell monolayers and the medium was changed to 5 % RPMI with 0.5 % P/S and an additional Mitomycin C [10 µg/mL] (10107409001, Roche, Germany). Mitomycin C served as a proliferation inhibitor. Cells were monitored using live cell imaging (Carl Zeiss, Oberkochen, Germany). Measurements were repeated accordingly with different CytoD-loaded FA-NP concentrations [1.5, 3.12, 6.25, and 12.5 µg/mL] to evaluate the concentration-dependent migration. Furthermore, measurements were performed in comparing the migration using FA-NP[CytoD] + Dynasore [5 µM] versus drug-unloaded FA-NP + Dynasore [5 µM].

4.14. Phagocytosis

Phagocytic activity of HMC-3 microglial cells was evaluated by measuring the uptake of pHrodo™ Red-conjugated *E. coli* bioparticles (pHrodo™ Red *E. coli* Bioparticles™, Thermo Fisher, Waltham, MA, USA), as previously described [97,99,102]. Cytochalasin D [5 µM] (#C2618, Sigma-Aldrich, Taufkirchen, Germany) was used as a negative control, whereas lipopolysaccharide [1 µg/mL] (from *Salmonella minnesota*, R596(Re) (TLRgrade™), ALX-581-008-L002, Enzo, Farmingdale, NY, USA) served as a positive control. Phagocytic activity was assessed at 24 h and 48 h following a 1-h incubation with either NaCl (control), FA-NP [6.25 µg/mL], FA-NP[CytoD] [6.25 µg/mL], molecular CytoD [5 µM], or LPS [1 µg/mL] (positive control). For this, cells were incubated with pHrodo™ Red *E. coli* Bioparticles™ for 1 h, followed by three washes with PBS medium. Quantification was performed by counting pHrodo™-positive cells per 1000 cells in each experimental condition [97].

4.15. Organotypic murine brain slice cultures

Organotypic brain slice cultures were prepared from adult female mice. All experimental procedures described in this manuscript were approved by the District Government of North Rhine Westphalia in Recklinghausen, Germany (LANUV ID 84-20.04.2015.A292), and all experiments involving animals were conducted in accordance with the ARRIVE guidelines from the NC3Rs (National Center for the Replacement, Refinement & Reduction of Animals in Research). Coronal brain slices with a thickness of 350 µm were prepared using a vibrating-blade microtome (Leica VT1200 S) and maintained in ice-cold, carbonated artificial cerebrospinal fluid (aCSF) during processing. For cultivation, the slices were placed onto 30 mm Millicell-CM tissue culture inserts with 0.4 µm pore size (Millipore) positioned in six-well culture plates containing long-term aCSF. Slices were maintained under membrane-interface conditions at the air-liquid interface, an established approach that improves oxygen availability and supports long-term viability of organotypic brain slices within this thickness range. Cultures were then incubated at 37 °C with 5 % CO_2 in a HERAcell cell culture incubator (Thermo Fisher). 350 µm formalin fixed organotypic adult murine brain slices were incubated in 10 % sucrose for several hours, followed by incubation in 30 % sucrose overnight. Subsequently, 12 µm coronal brain sections were prepared using a cryostat (Leica CM 3050S, Wetzlar, Germany) and directly mounted onto microscope slides. After washing in PBS, the slides were blocked with a blocking buffer (3 % normal goat serum in PBS) for 30 min. Then, they were incubated with the primary antibody, diluted in PBS (Table 2), overnight at 4 °C. The following day, the slides were washed in PBS and the secondary antibody (Table 2), diluted in PBS (1:500), was applied for 1 h at room temperature. Nuclear counterstaining was performed by incubating the slides in DAPI (4′,6-diamidino-2-phenylindole) for 1 min. After a final wash in PBS, the slides were mounted using Fluoromount-G.

4.16. Brain injury models

Hypoxia-Reoxygenation: To mimic ischemic stroke, we performed Oxygen-Glucose-Deprivation (OGD) as previously described [97], using 350 µm thick coronal organotypic adulte murine brain slice cultures. The applied OGD paradigm was selected based on established organotypic brain slice culture models of ischemia/hypoxia previously reported for whole hemisphere, hippocampal, cortical, and neurovascular slice systems [103–106]. Slices were maintained on membrane inserts for 24 h prior to hypoxic stimulation. Both aCSF and long-term aCSF contained 25 mM sodium hydrogen carbonate were adjusted to pH 7.4 before use. Oxygen depletion was induced in our customized hypoxia chamber (Part#: C174, C21, BioSpherix, Parish, NY, United States) by flooding the chamber with 100 % inert nitrogen gas until the oxygen concentration reached <1 %. To ensure stable OGD-conditions we monitored oxygen levels, temperature and pressure within the chamber. An additional oxygen sensor was used to monitor the oxygen level in the media (#200001735, PreSens, Regensburg, Germany). An orbital shaker was placed beneath the hypoxia chamber at 30 rpm ensuring better O_2 depletion in the media. The chamber itself was placed in a humidified incubator set to 37 °C. Normoxia controls were kept at 37 °C, 5 % CO_2 and atmospheric pressure. For hypoxia-reoxygenation experiments, slices were exposed to 30 min OGD/hypoxia. FA-NPs or FA-NP [CytoD] were applied *via* the surrounding culture medium at a concentration of 6.25 µg/mL for 1 h.

Focal Thermocoagulation: To mimic traumatic brain injury, we used a focal thermocoagulation injury model targeting the primary and secondary motor cortex, with involvement of both cortical and subcortical regions, including the corpus callosum using 350 µm thick coronal organotypic adulte murine brain slice cultures.

4.17. Animal experiments

All animal experiments were approved by the appropriate German authorities (LANUV: Landesamt für Natur, Umwelt und Verbraucherschutz Nordrhein-Westfalen) in accordance with national regulations. Six NOD/SCID female mice were purchased from Janvier Laboratories (NOD.CB17-Prkdc$^{scid/scid}$/Rj). The animals were housed in the Department of Nuclear Medicine of the University Hospital RWTH Aachen under a 12-h-light/12-h-dark cycle and were given *ad libitum* access to feed and water. The room temperature and relative humidity were kept between 20 and 25 °C and 45–65 %, respectively.

4.18. In vivo biodistribution

Mice were imaged with a small animal SPECT/CT system (X-CUBE and γ-CUBE, Molecubes, Gent, Belgium) as previously described [51]. Under 1.5 to 2.5 % isoflurane anesthesia in oxygen at 0.8 L/min, the lateral tail vein was injected with 30 MBq of [^{177}Lu]Lu-DOTA-FA-NPs [0.1 mg/mouse] diluted in 0.9 % NaCl to a total volume of 125 µL and scanned 4 h or 24 h post-injection. CT acquisition settings: Default high resolution protocol, 440 µA, 50 kVp, and 32 ms exposure time; the duration of each CT scan was approx. 5 min. The SPECT scan was initiated at the end of the CT. SPECT acquisition settings used: 7-headed

camera equipped with a general-purpose collimator with 28 pinholes (0.75 mm apertures and a radius of rotation of 20 mm) and a total duration of 30 min. During the scans, the isoflurane concentration was adapted to achieve a respiratory rate between 75 and 50 breaths per min. CT images were reconstructed as previously described [51], using an iterative reconstruction algorithm (ISRA) reconstruction process to an isometric voxel size of 0.2 mm in a 200 × 200 × 425 matrix. Using a vendor software, CT values were converted into Hounsfield units (HU) using the formula:

$$HU = 1000 \times ((\mu_t - \mu_w) \ / \ (\mu_w - \mu_a),$$

where μ_w is the linear attenuation coefficient of water, μ_a is the linear attenuation coefficient of air water and μ_t is the linear attenuation coefficient of the tissue. SPECT data were reconstructed using a 3-dimensional maximum likelihood estimation method (MLEM-3D with 50 iterations) into a 141 × 141 × 425 image matrix (resulting in final isometric voxel size of 0.25 mm) with an energy window of ±10 % from a peak of 113 keV and of 210 keV. SPECT and CT images were automatically aligned after reconstruction. PMOD software package version 3.13 (PMOD Technologies LLC, Zürich, Switzerland) was used to view, render, and analyze the SPECT/CT data. For the 3D rendering of the brain soft tissue, the inner side of the skull and vertebral canal was auto-segmented using a CT-based thresholding at 700 HU. Afterwards the outside of the auto-contour was masked, while the inside was used for 3D rendering using the P3D tool. The IN RANGE segmentation method was applied with −100 HU and 700 HU as limits, resulting in a single volume rendered object of the brain soft tissue. The co-registered SPECT acquisition was used as texture, with 0 and 800 prop. to cnts/sec as limits, using a Hot color scale. For the maximal intensity projection images (MIP), the PFUS tool was used with the following settings: for CT, the limits were set to 1 % and 100 % of the minimal and maximal HU value, while for SPECT the limits were set at 0 and 3100 prop. to cnts/sec.

Brains (24 h or 120 h p.i.) were perfused with PBS to remove residual blood, fixed, harvested and cut into 8 (2 mm thick) coronal brain sections. They were collected in γ-Counter test tubes, and their radioactivity was measured using a γ-Counter (Wizard^2, PerkinElmer, Waltham, USA) with a protocol for ^{177}Lu calibration. Radioactivity was then expressed as counts per minute (CPM). Thereafter, the coronal brain sections were placed on imaging plates (Fuji Film BAS-IP SR 2025, Raytest, Germany) for 24 h at room temperature and subsequently scanned using the Typhoon FLA 7000 (GE Healthcare, IL, USA) to visualize the ^{177}Lu-FA-NPs distribution by ARG prior to IHC analysis of FITC-FA-NPs in the same brain sections (Table 2).

4.19. Statistics

We utilized GraphPad Prism (version 8.4.3, San Diego, USA) for data analysis and visualization. Residuals were analyzed for normal distribution using the Shapiro-Wilk and D'Agostino-Pearson omnibus normality test. Variance homogeneity was tested using the Bartlett test or the Spearman's rank correlation test for heteroscedasticity. We utilized a ROUT test to identify outliers. $P < 0.05$ was considered statistically significant. Detailed description of biological and technical numbers are given in the corresponding figure legends including the statistical tests employed.

Declaration of AI use

The author(s) used LLMs, such as ChatGPT, for rephrasing and grammar editing. After using this tool, the author(s) reviewed and edited the content as needed and take(s) full responsibility for the content of the published article. AI was not used to generate or interpret data, and all output was double-checked and confirmed by the authors.

CRediT authorship contribution statement

Sabri E.M. Sahnoun: Data curation, Formal analysis, Investigation, Methodology, Visualization, Writing – original draft. **Rozina Noristani:** Data curation, Investigation, Writing – review & editing. **Paolo Alimonti:** Data curation, Investigation, Writing – review & editing. **Jonas Pes:** Investigation, Validation, Writing – review & editing. **Lara Gubeljak:** Investigation, Validation, Writing – review & editing. **Annika Szymura:** Investigation, Validation, Writing – review & editing. **Shaista Ilyas:** Investigation, Validation, Writing – review & editing. **Eren Arik:** Investigation, Validation, Writing – review & editing. **Alexandru Florea:** Investigation, Validation, Writing – review & editing. **Eva M. Buhl:** Investigation, Validation, Writing – review & editing. **Bernd Neumaier:** Methodology, Writing – review & editing. **Sanjay Mathur:** Resources, Writing – review & editing. **Jörg B. Schulz:** Resources, Writing – review & editing. **Felix M. Mottaghy:** Resources, Writing – review & editing. **Pardes Habib:** Conceptualization, Formal analysis, Funding acquisition, Investigation, Methodology, Project administration, Resources, Supervision, Writing – review & editing.

Declaration of competing interest

The authors declare the following financial interests/personal relationships which may be considered as potential competing interestsPardes Habib reports financial support was provided by German Research Foundation. Pardes Habib reports a relationship with University Hospital Aachen that includes: funding grants. This work was funded by an internal grant (START grant 111/17, Pardes habib) and the German Research Foundation (DFG), HA 9566/1-1 (Pardes Habib) and supported by the "Clinician Scientist program" of the Faculty of Medicine, RWTH Aachen University (Pardes Habib) If there are other authors, they declare that they have no known competing financial interests or personal relationships that could have appeared to influence the work reported in this paper.

Acknowledgements and Funding

We thank Sabine Hamm, Fiona Teubner (Department of Neurology, Medical Faculty, RWTH Aachen University) for their excellent technical assistance. We thank Patrick Robert Buchta from the Audiovisual Media Center (AVMZ), Medical Faculty, RWTH Aachen University, for his support with the graphical visualization of the nanoparticles. We thank the workgroup of Prof. Jahnen-Dechent (Helmholtz Institute for Biomedical Engineering, Biointerface Laboratory, RWTH Aachen University) for their technical support in the NTA analysis. This work was funded by an internal grant (START grant 111/17, PH) and the German Research Foundation (DFG), HA 9566/1-1 (PH) and supported by the "Clinician Scientist program" of the Faculty of Medicine, RWTH Aachen University (PH). The funding body had no influence on the design of the study, data acquisition or on analyses and interpretation of data.

Appendix A. Supplementary data

Supplementary data to this article can be found online at https://doi.org/10.1016/j.biomaterials.2026.124495.

Data availability

Data will be made available on request.

References

[1] J.D. Steinmetz, et al., Global, regional, and national burden of disorders affecting the nervous system, 1990–2021: a systematic analysis for the global burden of disease study 2021, Lancet Neurol. 23 (2024) 344–381.
[2] V.L. Feigin, et al., The global burden of neurological disorders: translating evidence into policy, Lancet Neurol. 19 (2020) 255–265.

[3] X. Li, et al., Global, regional, and national burden of ischemic stroke, 1990–2021: an analysis of data from the global burden of disease study 2021, eClinicalMedicine 75 (2024) 102758.
[4] R. Pandit, L. Chen, J. Götz, The blood-brain barrier: physiology and strategies for drug delivery, Adv. Drug Deliv. Rev. 165–166 (2020) 1–14.
[5] W.A. Banks, From blood–brain barrier to blood–brain interface: new opportunities for CNS drug delivery, Nat. Rev. Drug Discov. 15 (2016) 275–292.
[6] D. Wu, et al., The blood–brain barrier: structure, regulation and drug delivery, Signal Transduct. Targeted Ther. 8 (2023) 217.
[7] N.B. Ndemazie, et al., Multi-disciplinary approach for drug and gene delivery systems to the brain, AAPS PharmSciTech 23 (2022) 11.
[8] V. Saini, L. Guada, D.R. Yavagal, Global epidemiology of stroke and access to acute ischemic stroke interventions, Neurology 97 (2021).
[9] H.M. Tiesman, S. Konda, J.L. Bell, The epidemiology of fatal occupational traumatic brain injury in the U.S, Am. J. Prev. Med. 41 (2011) 61–67.
[10] S. Bachiller, et al., Microglia in neurological diseases: a road map to brain-disease dependent-inflammatory response, Front. Cell. Neurosci. 12 (2018) 488.
[11] S.C. Woodburn, J.L. Bollinger, E.S. Wohleb, The semantics of microglia activation: neuroinflammation, homeostasis, and stress, J. Neuroinflammation 18 (2021) 258.
[12] H. Kettenmann, U.-K. Hanisch, M. Noda, A. Verkhratsky, Physiology of microglia, Physiol. Rev. 91 (2011) 461–553.
[13] D.J. Loane, A. Kumar, Microglia in the TBI brain: the good, the bad, and the dysregulated, Exp. Neurol. 275 (2016) 316–327.
[14] R.C. Paolicelli, et al., Microglia states and nomenclature: a field at its crossroads, Neuron 110 (2022) 3458–3483.
[15] S.E. Hickman, et al., The microglial sensome revealed by direct RNA sequencing, Nat. Neurosci. 16 (2013) 1896–1905.
[16] S. Lively, L.C. Schlichter, Microglia responses to pro-inflammatory stimuli (LPS, IFNγ+TNFα) and reprogramming by resolving cytokines (IL-4, IL-10), Front. Cell. Neurosci. 12 (2018) 215.
[17] J.D. Cherry, J.A. Olschowka, M.K. O'Banion, Neuroinflammation and M2 microglia: the good, the bad, and the inflamed, J. Neuroinflammation 11 (2014) 98.
[18] R. Orihuela, C.A. McPherson, G.J. Harry, Microglial M1/M2 polarization and metabolic states, Br. J. Pharmacol. 173 (2016) 649–665.
[19] X. Hu, et al., Microglia/macrophage polarization dynamics reveal novel mechanism of injury expansion after focal cerebral ischemia, Stroke 43 (2012) 3063–3070.
[20] K.A. Kigerl, et al., Identification of two distinct macrophage subsets with divergent effects causing either neurotoxicity or regeneration in the injured mouse spinal cord, J. Neurosci. 29 (2009) 13435–13444.
[21] L. Xu, J. Wang, Y. Ding, L. Wang, Y.-J. Zhu, Current knowledge of microglia in traumatic spinal cord injury, Front. Neurol. 12 (2022) 796704.
[22] D.J. Loane, K.R. Byrnes, Role of microglia in neurotrauma, Neurotherapeutics 7 (2010) 366–377.
[23] M. Fumagalli, M. Lombardi, P. Gressens, C. Verderio, How to reprogram microglia toward beneficial functions, Glia 66 (2018) 2531–2549.
[24] J.F. Casella, M.D. Flanagan, S. Lin, Cytochalasin D inhibits actin polymerization and induces depolymerization of actin filaments formed during platelet shape change, Nature 293 (1981) 302–305.
[25] M. Fricker, M.J. Oliva-Martín, G.C. Brown, Primary phagocytosis of viable neurons by microglia activated with LPS or Aβ is dependent on calreticulin/LRP phagocytic signalling, J. Neuroinflammation 9 (2012) 697.
[26] O.M. Mitrasinovic, G.M. Murphy, Accelerated phagocytosis of Amyloid-β by mouse and human microglia overexpressing the macrophage colony-stimulating factor receptor, J. Biol. Chem. 277 (2002) 29889–29896.
[27] M. Trendowski, V. Wong, K. Wellington, S. Hatfield, T.P. Fondy, Tolerated doses in zebrafish of cytochalasins and jasplakinolide for comparison with tolerated doses in mice in the evaluation of pre-clinical activity of microfilament-directed agents in tumor model systems in vivo, Vivo Athens Greece 28 (2014) 1021–1031.
[28] A. Chen, S. Wang, W. Cai, Z. Mu, Y. Chen, Tunable synthesis, characterization, and CMP performance of dendritic mesoporous silica nanospheres as functionalized abrasives, Colloids Surf. A Physicochem. Eng. Asp. 638 (2022) 128322.
[29] F. Rizzi, et al., High surface area mesoporous silica nanoparticles with tunable size in the sub-micrometer regime: insights on the size and porosity control mechanisms, Molecules 26 (2021) 4247.
[30] M.A. Taha, R.A. Youness, M. Ibrahim, Biocompatibility, physico-chemical and mechanical properties of hydroxyapatite-based silicon dioxide nanocomposites for biomedical applications, Ceram. Int. 46 (2020) 23599–23610.
[31] R. Khoz, et al., Current trends in silica based drug delivery systems, Eur. J. Med. Chem. Rep 12 (2024) 100206.
[32] L. Chen, et al., The toxicity of silica nanoparticles to the immune system, Nanomed 13 (2018) 1939–1962.
[33] T. Hirai, et al., Size-dependent immune-modulating effect of amorphous nanosilica particles, Pharm. Times 66 (2011) 727–728.
[34] F. Sánchez-Cano, L.C. Hernández-Kelly, A. Ortega, Silica nanoparticles decrease glutamate uptake in blood–brain barrier components, Neurotox. Res. 42 (2024) 20.
[35] J. Choi, Q. Zheng, H.E. Katz, T.R. Guilarte, Silica-based nanoparticle uptake and cellular response by primary microglia, Environ. Health Perspect. 118 (2010) 589–595.
[36] Y. Xue, J. Wu, J. Sun, Four types of inorganic nanoparticles stimulate the inflammatory reaction in brain microglia and damage neurons in vitro, Toxicol. Lett. 214 (2012) 91–98.
[37] S. Hou, et al., Silica nanoparticles cause activation of NLRP3 inflammasome in-vitro model-using microglia, Int. J. Nanomed. 17 (2022) 5247–5264.
[38] K. Boukholda, et al., Subacute silica nanoparticle exposure induced oxidative stress and inflammation in rat hippocampus combined with disruption of cholinergic system and behavioral functions, NanoImpact 24 (2021) 100358.
[39] W. Wei, et al., Brain accumulation and toxicity profiles of silica nanoparticles: the influence of size and exposure route, Environ. Sci. Technol. 56 (2022) 8319–8325.
[40] S. Acter, M. Moreau, R. Ivkov, A. Viswanathan, W. Ngwa, Polydopamine nanomaterials for overcoming current challenges in cancer treatment, Nanomaterials 13 (2023) 1656.
[41] W. Lei, et al., Polydopamine-coated mesoporous silica nanoparticles for multi-responsive drug delivery and combined chemo-photothermal therapy, Mater. Sci. Eng. C 105 (2019) 110103.
[42] Q. Zheng, et al., Mussel-inspired polydopamine coated mesoporous silica nanoparticles as pH-sensitive nanocarriers for controlled release, Int. J. Pharm. 463 (2014) 22–26.
[43] X. Tang, et al., pH-Responsive magnetic mesoporous silica-based nanoplatform for synergistic photodynamic therapy/chemotherapy, ACS Appl. Mater. Interfaces 10 (2018) 15001–15011.
[44] Y. Cheng, et al., Polydopamine-coated manganese carbonate nanoparticles for amplified magnetic resonance imaging-guided photothermal therapy, ACS Appl. Mater. Interfaces 9 (2017) 19296–19306.
[45] Q. Yue, et al., A versatile ethanol-mediated polymerization of dopamine for efficient surface modification and the construction of functional core–shell nanostructures, J. Mater. Chem. B 1 (2013) 6085.
[46] J. Hu, et al., Asn-Gly-Arg-modified polydopamine-coated nanoparticles for dual-targeting therapy of brain glioma in rats, Oncotarget 7 (2016) 73681–73696.
[47] T. Zhu, et al., Melanin-like polydopamine nanoparticles mediating anti-inflammatory and rescuing synaptic loss for inflammatory depression therapy, J. Nanobiotechnol. 21 (2023) 52.
[48] P. Elo, et al., Folate receptor-targeted positron emission tomography of experimental autoimmune encephalomyelitis in rats, J. Neuroinflammation 16 (2019) 252.
[49] C. Tronel, et al., Molecular targets for PET imaging of activated microglia: the current situation and future expectations, Int. J. Mol. Sci. 18 (2017) 802.
[50] K.S. MacDowell, et al., The atypical antipsychotic paliperidone regulates endogenous Antioxidant/anti-inflammatory pathways in rat models of acute and chronic restraint stress, Neurotherapeutics 13 (2016) 833–843.
[51] S. Ilyas, et al., Validation of dual-action chemo-radio-labeled nanocarriers with high efficacy against triple-negative breast cancer, ACS Appl. Mater. Interfaces 15 (2023) 48963–48977.
[52] R. Muralidharan, et al., Folate receptor-targeted nanoparticle delivery of HuR-RNAi suppresses lung cancer cell proliferation and migration, J. Nanobiotechnol. 14 (2016) 47.
[53] A.A. Lohade, et al., A novel folate-targeted nanoliposomal system of doxorubicin for cancer targeting, AAPS PharmSciTech 17 (2016) 1298–1311.
[54] H. Wang, et al., Inhibitor analysis revealed that clathrin-mediated endocytosis is involed in cellular entry of type III grass carp reovirus, Virol. J. 15 (2018) 92.
[55] L. Brannon-Peppas, Recent advances on the use of biodegradable microparticles and nanoparticles in controlled drug delivery, Int. J. Pharm. 116 (1995) 1–9.
[56] S. Kwon, et al., Silica-based mesoporous nanoparticles for controlled drug delivery, J. Tissue Eng. 4 (2013) 2041731413503357.
[57] C. Bharti, N. Gulati, U. Nagaich, A. Pal, Mesoporous silica nanoparticles in target drug delivery system: a review, Int. J. Pharm. Investig. 5 (2015) 124.
[58] K.B. Seljak, P. Kocbek, M. Gašperlin, Mesoporous silica nanoparticles as delivery carriers: an overview of drug loading techniques, J. Drug Deliv. Sci. Technol. 59 (2020) 101906.
[59] I.I. Slowing, C. Wu, J.L. Vivero-Escoto, V.S.-Y. Lin, Mesoporous silica nanoparticles for reducing hemolytic activity towards mammalian red blood cells, Small 5 (2009) 57–62.
[60] S. Jafari, et al., Mesoporous silica nanoparticles for therapeutic/diagnostic applications, Biomed. Pharmacother. 109 (2019) 1100–1111.
[61] D. Napierska, et al., Size-dependent cytotoxicity of monodisperse silica nanoparticles in human endothelial cells, Small 5 (2009) 846–853.
[62] U. Niroumand, et al., The effect of size, morphology and surface properties of mesoporous silica nanoparticles on pharmacokinetic aspects and potential toxicity concerns, Front. Mater. 10 (2023) 1189463.
[63] S.M. Lombardo, M. Schneider, A.E. Türeli, N. Günday Türeli, Key for crossing the BBB with nanoparticles: the rational design, Beilstein J. Nanotechnol. 11 (2020) 866–883.
[64] C. Freitas, R.H. Müller, Effect of light and temperature on zeta potential and physical stability in solid lipid nanoparticle (SLN^{TM}) dispersions, Int. J. Pharm. 168 (1998) 221–229.
[65] Y. Tsou, X. Zhang, H. Zhu, S. Syed, X. Xu, Drug delivery to the brain across the blood–brain barrier using nanomaterials, Small 13 (2017) 1701921.
[66] P.R. Lockman, J.M. Koziara, R.J. Mumper, D.D. Allen, Nanoparticle surface charges alter blood–brain barrier integrity and permeability, J. Drug Target. 12 (2004) 635–641.
[67] B. Zhang, et al., LDLR-mediated peptide-22-conjugated nanoparticles for dual-targeting therapy of brain glioma, Biomaterials 34 (2013) 9171–9182.

[68] Y.-P. Chen, et al., Bridging size and charge effects of mesoporous silica nanoparticles for crossing the blood–brain barrier, Front. Chem. 10 (2022) 931584.
[69] J.M. Rosenholm, C. Sahlgren, M. Lindén, Towards multifunctional, targeted drug delivery systems using mesoporous silica nanoparticles – opportunities & challenges, Nanoscale 2 (2010) 1870.
[70] T. Liu, et al., Single and repeated dose toxicity of mesoporous hollow silica nanoparticles in intravenously exposed mice, Biomaterials 32 (2011) 1657–1668.
[71] J. Rejman, V. Oberle, I.S. Zuhorn, D. Hoekstra, Size-dependent internalization of particles via the pathways of clathrin- and caveolae-mediated endocytosis, Biochem. J. 377 (2004) 159–169.
[72] M.-O. Parat, G.J. Riggins, Caveolin-1, caveolae, and glioblastoma, Neuro Oncol. 14 (2012) 679–688.
[73] N. Gennet, C. Tamburini, X. Nan, M. Li, FolR1: a novel cell surface marker for isolating midbrain dopamine neural progenitors and nascent dopamine neurons, Sci. Rep. 6 (2016) 32488.
[74] V. Sangha, Md T. Hoque, J.T. Henderson, R. Bendayan, Novel localization of folate transport systems in the murine central nervous system, Fluids Barriers CNS 19 (2022) 92.
[75] O.A. Balashova, O. Visina, L.N. Borodinsky, Folate receptor 1 is necessary for neural plate cell apical constriction during *Xenopus* neural tube formation, Development 144 (2017) 1518–1530.
[76] O.A. Balashova, et al., Noncanonical function of folate through folate receptor 1 during neural tube formation, Nat. Commun. 15 (2024) 1642.
[77] S.G. Utz, et al., Early fate defines microglia and non-parenchymal brain macrophage development, Cell 181 (2020) 557–573.e18.
[78] K. Siletti, et al., Transcriptomic diversity of cell types across the adult human brain, Science 382 (2023) eadd7046.
[79] A. Chen, et al., Spatiotemporal transcriptomic atlas of mouse organogenesis using DNA nanoball-patterned arrays, Cell 185 (2022) 1777–1792.e21.
[80] L. Liu, et al., Spatiotemporal omics for biology and medicine, Cell 187 (2024) 4488–4519.
[81] L. Cao, et al., Uncovering the interplay between pH receptors and immune cells: potential drug targets, Oncol. Rep. 46 (2021) 228 (Review).
[82] B.G. Trewyn, J.A. Nieweg, Y. Zhao, V.S.-Y. Lin, Biocompatible mesoporous silica nanoparticles with different morphologies for animal cell membrane penetration, Chem. Eng. J. 137 (2008) 23–29.
[83] F. Lu, S. Wu, Y. Hung, C. Mou, Size effect on cell uptake in well-suspended, uniform mesoporous silica nanoparticles, Small 5 (2009) 1408–1413.
[84] S. Mayor, R.E. Pagano, Pathways of clathrin-independent endocytosis, Nat. Rev. Mol. Cell Biol. 8 (2007) 603–612.
[85] M. Gisbert-Garzarán, et al., Designing mesoporous silica nanoparticles to overcome biological barriers by incorporating targeting and endosomal escape, ACS Appl. Mater. Interfaces 13 (2021) 9656–9666.
[86] S.A. Smith, L.I. Selby, A.P.R. Johnston, G.K. Such, The endosomal escape of nanoparticles: toward more efficient cellular delivery, Bioconjug. Chem. 30 (2019) 263–272.
[87] J. Gao, et al., Intracerebral fate of organic and inorganic nanoparticles is dependent on microglial extracellular vesicle function, Nat. Nanotechnol. 19 (2024) 376–386.
[88] A.J. Di Pasqua, et al., Cytotoxicity of mesoporous silica nanomaterials, J. Inorg. Biochem. 102 (2008) 1416–1423.
[89] Q. He, et al., A pH-responsive mesoporous silica nanoparticles-based multi-drug delivery system for overcoming multi-drug resistance, Biomaterials 32 (2011) 7711–7720.
[90] G. Xie, J. Sun, G. Zhong, L. Shi, D. Zhang, Biodistribution and toxicity of intravenously administered silica nanoparticles in mice, Arch. Toxicol. 84 (2010) 183–190.
[91] W. Najahi-Missaoui, R.D. Arnold, B.S. Cummings, Safe nanoparticles: are we there yet? Int. J. Mol. Sci. 22 (2020) 385.
[92] S. Sotoma, Polyglycerol/polydopamine-coated nanoparticles for biomedical applications, Front. Mater. 9 (2022) 878455.
[93] I. Singh, G. Dhawan, S. Gupta, P. Kumar, Recent advances in a polydopamine-mediated antimicrobial adhesion system, Front. Microbiol. 11 (2021) 607099.
[94] M. Trendowski, J.M. Mitchell, C.M. Corsette, C. Acquafondata, T.P. Fondy, Chemotherapy in vivo against M109 murine lung carcinoma with cytochalasin B by localized, systemic, and liposomal administration, Invest. New Drugs 33 (2015) 280–289.
[95] D. Chang, et al., Polydopamine-based surface modification of mesoporous silica nanoparticles as pH-sensitive drug delivery vehicles for cancer therapy, J. Colloid Interface Sci. 463 (2016) 279–287.
[96] S. Ilyas, et al., Mediating the fate of cancer cell uptake: dual-targeted magnetic nanovectors with biotin and folate surface ligands, ACS Biomater. Sci. Eng. 6 (2020) 6138–6147.
[97] E. Arik, et al., Erythropoietin enhances post-ischemic migration and phagocytosis and alleviates the activation of inflammasomes in human microglial cells, Front. Cell. Neurosci. 16 (2022) 915348.
[98] T. Zeyen, et al., Microglial-specific depletion of TAK1 is neuroprotective in the acute phase after ischemic stroke, J. Mol. Med. 98 (2020) 833–847.
[99] P. Habib, et al., Regulation of hypoxia-induced inflammatory responses and M1-M2 phenotype switch of primary rat microglia by sex steroids, J. Mol. Neurosci. 52 (2014) 277–285.
[100] P. Habib, D. Dreymueller, A. Ludwig, C. Beyer, J. Dang, Sex steroid hormone-mediated functional regulation of microglia-like BV-2 cells during hypoxia, J. Steroid Biochem. Mol. Biol. 138 (2013) 195–205.
[101] M.W. Pfaffl, A new mathematical model for relative quantification in real-time RT-PCR, Nucleic Acids Res. 29 (2001) 45e–445.
[102] P. Habib, J. Harms, A. Zendedel, C. Beyer, A. Slowik, Gonadal hormones E2 and P mitigate cerebral ischemia-induced upregulation of the AIM2 and NLRC4 inflammasomes in rats, Int. J. Mol. Sci. 21 (2020) 4795.
[103] M. McKenna, et al., Organotypic whole hemisphere brain slice models to study the effects of donor age and oxygen-glucose-deprivation on the extracellular properties of cortical and striatal tissue, J. Biol. Eng. 16 (2022) 14.
[104] L. Wise-Faberowski, P.N. Robinson, S. Rich, D.S. Warner, Oxygen and glucose deprivation in an organotypic hippocampal slice model of the developing rat brain: the effects on N-Methyl-d-Aspartate subunit composition, Anesth. Analg. 109 (2009) 205–210.
[105] M. Ziemka-Nałęcz, L. Stanaszek, T. Zalewska, Oxygen-glucose deprivation promotes gliogenesis and microglia activation in organotypic hippocampal slice culture: involvement of metalloproteinases, Acta Neurobiol. Exp. 73 (2013) 130–142.
[106] S. Fujimoto, H. Katsuki, T. Kume, S. Kaneko, A. Akaike, Mechanisms of oxygen glucose deprivation-induced glutamate release from cerebrocortical slice cultures, Neurosci. Res. 50 (2004) 179–187.